Multiscale Acoustic Properties of Nanoporous Materials: From Microscopic Dynamics to Mechanics and Wave Propagation

Alan Sam, Marina Barbagero Álvarez, Rodolfo Venegas, Benoit Coasne

Multiscale Acoustic Properties of Nanoporous Materials: From Microscopic Dynamics to Mechanics and Wave Propagation

Alan Sam,[†] Marina Barbagero Álvarez,[†] Rodolfo Venegas,[*,‡] and Benoit Coasne[*,†]

[†] *Universitè Grenoble Alpes, CNRS, LIPhy, 38000, Grenoble, France*

[‡] *University Austral of Chile, Institute of Acoustics, P.O. Box 567, Valdivia, Chile*

E-mail: rodolfo.venegas@uach.cl; benoit.coasne@univ-grenoble-alpes.fr

Abstract

Despite significant progress in deciphering the mechanical properties of nanoporous materials, the intimately-related phenomenon of acoustic wave propagation in such solids remains largely unexplored at this vanishing length scale (i.e. the molecular scale). Here, we report a multiscale approach to estimate the acoustic properties of zeolites – a prototypical class of nanoporous materials – by combining molecular dynamics simulations and a rigorous upscaling approach using continuum mechanics. Two different zeolites are considered, *i.e.* RHO and JST zeolites; while they share a simple yet different crystallographic structure, the latter shows auxeticity. First, microscopic simulations are used to calculate the speed of sound from the phonon spectrum as obtained using molecular displacement and velocity data. As an alternate route, macroscopic mechanical constants of the materials are also determined to confirm the

inferred acoustic velocities by solving the Kelvin-Christoffel equation. With the second approach, the data are obtained using either the strain fluctuations in a simulation performed at equilibrium or from the slope of the stress-strain curve assessed using simple mechanical tests. Second, we propose a nano-to-macro modelling strategy in which the inputs for the continuum-level upscaled model are the specific outcomes from the molecular calculations (*e.g.* speeds of sound, mechanical parameters). This strategy allows determining the acoustic properties of an empty double porosity material formed by adding an extra scale of porosity to a nanoporous skeleton. Such extra scale of porosity can represent larger pores, voids in between consolidated nanoporous grains, and/or possible large defects or microfractures in the nanoporous skeleton whose effects can be probed by acoustic waves. This work paves the way for further studies in the field of nanoscale acoustics – especially in the context of applications involving nanoporous materials.

1. Introduction

Nanoporous materials are either crystalline or amorphous solids displaying a porous morphology with pore diameters ranging from ∼1 nm to 100 nm.[1–3] Owing to strong confinement and surface effects in their very narrow porosity, this class of materials keeps receiving interest in various fields relevant to both science and engineering. From a fundamental viewpoint, when confined to nanoscale dimensions such as in nanoporous materials, fluids exhibit unique thermodynamic and dynamical properties that are drastically influenced by the surface forces and confinement effects.[2,4–7] From a practical viewpoint, the large surface-to-volume ratio, large porosity and narrow pore size in nanoporous materials make them ideal candidates for many functional applications such as in adsorption, catalysis, sensing, separation, *etc.*[8] Beyond such applications, nanoporous materials like natural zeolites are also used for important practical implementations relying on their mechanical properties.[9–12] This includes applications such as mixing with concrete, which was found to improve the durability and

permeability of concrete while reducing its overall weight.[13] Moreover, there has also been considerable interest in the compressibility[14–17] or collapse[18–20] of nanoporous materials – either empty or filled with an adsorbed fluid – to design shock absorbers, energy storage devices, or molecular springs. In particular, the mechanical properties of zeolites have been shown to display pressure-induced amorphization with a pressure threshold that can be tuned by inserting fluids inside their nanoporosity.[21,22]

Despite unquestionable advantages linked to their low weight-to-strength ratio, nanoporous structures can undergo significant mechanical deformations – especially upon guest molecule adsorption within their porosity. On the one hand, for dense materials, many experimental and theoretical studies have unraveled the mechanisms underlying their mechanical behavior and deformation.[23] On the other hand, for porous materials – especially with nanoscale pore dimensions, an understanding of the fundamental microscopic phenomena involved in mechanical deformation is still lacking. While significant progress has been made in the field of poromechanics involving fluid adsorption and the associated mechanical deformation,[24–28] the intrinsic molecular mechanisms involved in deformation and, generally, mechanical solicitation remains to be fully explored. In this context, one of the major challenges associated with this knowledge gap on nanoporous materials is to better understand acoustic wave propagation in their heterogeneous structure. Considering the intrinsic molecular, i.e. nanoscopic, length scale inherent to physical phenomena in these nanostructures, many questions remain unanswered regarding the acoustic properties of this class of materials. A fundamental understanding of acoustic wave propagation in these nanoporous media is highly interesting with many potential applications in the field of acoustics (*e.g.* sound absorbers,[29,30] sound insulators,[30,31] compliance enhancers,[32–34] shock absorbers[35,36]) and micro/nano-fluidics.[37]

To better understand the acoustic wave/matter interaction in nanoporous solids, this work uses molecular simulation and statistical mechanics tools, combined with a rigorous upscaling method, to predict and interpret the acoustic response of zeolites — which are considered here as prototypical nanoporous materials – as well as that of a double porosity

material whose skeleton is made of them. Two all-silica zeolites, which consist of nanoporous crystalline silica SiO_2 having a pore size of the order of a few Å to 1-2 nm, are considered. In more detail, we use two simple but representative cubic zeolite materials, *i.e.* RHO and JST zeolites – both having a 3-dimensional tetrahedral framework in which each oxygen atom is shared by two tetrahedra (consisting of silicon atoms connected to four oxygen atoms). While the cubic structure of RHO and JST zeolites considerably reduces the complexity of the problem under study, extension to more complex zeolitic systems is straightforward. Despite possessing a similar cubic structure, the mechanical properties of RHO and JST zeolites are significantly different. First, the bulk elastic modulus for RHO zeolite is about an order of magnitude higher than that for JST zeolite. In this respect, as shown in Fig. S1 in the Supporting Information, the mechanical properties (e.g. bulk modulus) vary broadly among zeolites even when restricting the data to cubic structures. This result suggests that the exact arrangement of atoms, i.e. molecular topology, in the crystal is a key parameter. Our choice to select RHO and JST zeolites is motivated by the fact that these materials possess very different mechanical properties (by orders of magnitude) which allows probing very different mechanical and, hence, acoustic behaviors. Second, another motivation for this choice comes from the fact that JST zeolite exhibits auxetic properties (negative Poisson's ratio) which is of high interest among researchers for both theoretical and practical aspects.[38–40]

On the one hand, both the mechanical and acoustic properties of media having pores with well distinct characteristic sizes, that are large enough for the continuum assumption to hold, have been thoroughly studied (see *e.g.* [41–48] for double porosity media). On the other hand, to the authors' knowledge, no attempt has ever been made to study, by combining molecular dynamics and continuum-based upscaling techniques, the acoustic properties of double porosity media in which the smallest pores are nanometric. This paper fills this gap.

We employ different routes to assess acoustic propagation in zeolite materials: (1) microscopic dynamics in which the sound velocity is derived from phonon calculations and (2) macroscopic mechanical constants to predict the longintudinal and transverse speeds of

sound. With the microscopic dynamics route, the dynamic structure factor is determined to assess, in turn, the speed of sound using a simple damped harmonic oscillator model. With the macroscopic route, the longitudinal and transverse speeds of sound are determined from the elasticity matrix. In this case, the mechanical constants are predicted consistently either from the strain fluctuations at equilibrium[49] or from tensile/shear mechanical tests. To do so, molecular simulation techniques — including molecular dynamics in the isobaric/isothermal ensemble — are employed to simulate the mechanical and acoustical response of a zeolite. With the knowledge of mechanical constants obtained from molecular dynamics, we calculate the longitudinal and transverse speeds of sound in different directions of acoustic wave propagation by applying Kelvin-Christoffel's equation. In the second part of this paper, the results of the molecular simulations are used in conjunction with the two-scale method of homogenization[50] to introduce an upscaled model of wave propagation in empty double porosity materials formed by adding an extra scale of porosity to a nanoporous skeleton. Such extra scale of porosity can represent, among others, larger pores, voids in between consolidated nanoporous grains, and/or possible large defects or microfractures in the nanoporous skeleton whose effects can be probed by acoustic waves. Our study provides important insights into the mechanical and dynamical properties to both prototypical nanoporous materials, such as the zeolites studied in this work, and those of multiscale media made out of them.

2. Computational Methods

2.1 Molecular models

We utilized the repository of the International Zeolite Association[51] to create molecular models for RHO and JST zeolites (Figure 1). The unit cells for these two cubic materials ($a = b = c$) are shown in Fig. 1(a) and (b). The lattice parameters are 14.919 Å for RHO zeolite and 14.979 Å for JST zeolite. To minimize finite size effects while performing simulations at a reasonable computational expense, a $3 \times 3 \times 3$ supercell was generated for

each zeolite by tripling (unless otherwise mentioned) the unit cell in each space direction and periodic boundary conditions were applied. The resulting supercell for RHO zeolite is shown in Fig. 1(c) (the same strategy was used for JST zeolite). Given the typical Si–O bond length ($d \sim 1.69$ Å), Si and O atoms were considered bonded in RHO and JST zeolites if the distance between them is less than 1.75 Å(with this number, we verified that each Si atom is bonded to 4 O atoms while each O atom is bonded to two Si atoms as expected in SiO_4 tetrahedra).

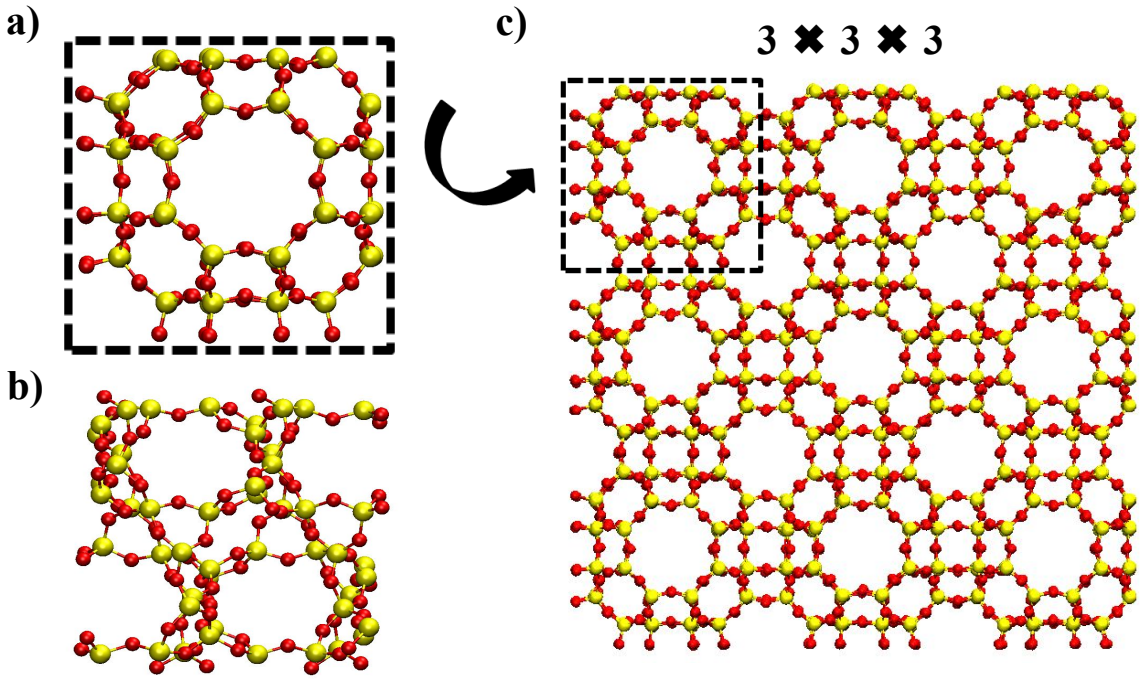

Figure 1: Unit cell for (a) RHO and (b) JST zeolites with silicon and oxygen atoms represented in yellow and red colors. The lattice parameter for RHO and JST zeolites are $a = 14.919$ Å and $a = 14.970$ Å, respectively. (c) 2D representation of the supercell of RHO zeolite created by tripling the unit cell in x, y and z directions.

2.2 Molecular dynamics

The RHO and JST zeolite supercells were initially relaxed for 1 ns at constant external stress σ and temperature T. An external stress of $\sigma = 1$ atm was imposed in each space direction – uncoupled in each direction – using a Parrinello-Rahman barostat with a relaxation time of

0.05 ps. To maintain the zeolite structure at a constant temperature $T = 300$ K, we employed a Nosé-Hoover thermostat with a relaxation time of 0.005 ps. As described in what follows, the equilibrated zeolite structures were then subjected to different simulation protocols: molecular dynamics (MD) simulations in either the NVT or $N\sigma T$ ensemble depending on the approach used for calculating the acoustic response of these nanoporous structures. In more detail, to estimate the speeds of sound via the microscopic dynamics route, we conducted MD simulations in the NVT ensemble on an elongated system by replicating the unit cells of RHO and JST zeolites 9 times in x-direction and 3 times in y and z-directions, respectively. The elongated box sizes of these nanoporous systems allow the evaluation of acoustic velocities for small wave vectors $\mathbf{q}$ as illustrated below. The use of such elongated boxes is important as the macroscopic speed of sound is only reached for small $\mathbf{q}$ vectors. In addition, using such MD simulations in the NVT ensemble, the phonon dynamics of the nanoporous materials were calculated by performing simulations for 300 ps and saving the trajectory of the zeolites every 0.0025 ps. With the macroscopic route, the acoustic velocity is predicted using the strain fluctuations approach with simulations performed at a constant external stress of 1 atm until the strain correlations converge. The trajectory was saved at time intervals of 1 ps for a running time of 8 ns. In an alternative macroscopic route, different mechanical tests – i.e. tensile and shear tests – were performed to determine mechanical constants and, in turn, the acoustic velocities for both RHO and JST zeolites. Typically, in the tensile test, the supercells (3×3×3) were deformed by stretching the system at a uniform rate along the x-direction. The zeolites were also subjected to a shear test by keeping the bottom of the zeolite fixed along the x-axis while a constant shearing along the x-direction at a uniform rate was applied to the top surface. In both mechanical tests, the strain rate applied was 1.0×10^{-6} s^{-1}. We conducted test simulations on five independent structural configurations to estimate statistical errors associated with the results obtained from the mechanical tests and fluctuations approach. All molecular simulations were carried out using the LAMMPS package[52] with a time step of 0.5 fs.

2.3 Force field

All intermolecular interactions were described using the force field proposed by Ghysels et al.[53] With this model, the force field considers explicitly Si-O, O-O and Si-Si interactions that are modelled using Lennard-Jones (LJ) interaction potentials. These Lennard-Jones potentials employed to model such interactions were truncated at a distance of 13 Å. The energy contribution from Si-O-Si and O-Si-O angles were described through harmonic functions while torsion was neglected. The partial charges on Si and O atoms in the zeolites were set to +2.1 e and -1.05 e, respectively. The long-range electrostatic interactions in the supercell were calculated using the particle-particle particle-mesh (PPPM) solver to an accuracy of 10^{-5}. We used a cut-off distance of 13 Å for computing the real space contribution of the electrostatic interactions.[54] The parameters used to model the LJ interactions are given in Table 1. Using the force field mentioned above, we observed the time evolution of lattice parameters a, b and c for RHO and JST zeolites, shown in Figure 2. The systems were allowed to relax in the NσT ensemble wherein the cubic symmetry of the zeolites is found to remain stable. The lattice parameters, a, b and c, in RHO and JST zeolites are 15.001 and 15.303 Å, respectively. The lattice parameters predicted in the study show excellent agreement with previous MD and DFT calculations.[55]

Table 1: Force field parameters used to model atomic interactions in RHO and JST zeolites. In addition to partial charges on zeolite atoms leading to an electrostatic contribution, the Si-O, O-O and Si-Si interactions are described using Lennard-Jones interaction potentials. The Si-O-Si and O-Si-O angles are described through harmonic functions (no torsion is considered as this contribution is included in an effective fashion in the other contributions).

Interaction (LJ)	A (eV.Å^{12})	B (eV.Å^{6})
Si-Si	0.5601	0.0004
O-O	26877.9664	29.8306
Si-O	172.6992	0.1086
Three-body (harmonic)	K_{ijk} (eV.Å^{-2})	$\theta_{0,\mathrm{ijk}}$ (°)
O-Si-O	1.4944	109.47
Si-O-Si	1.5509	142.71

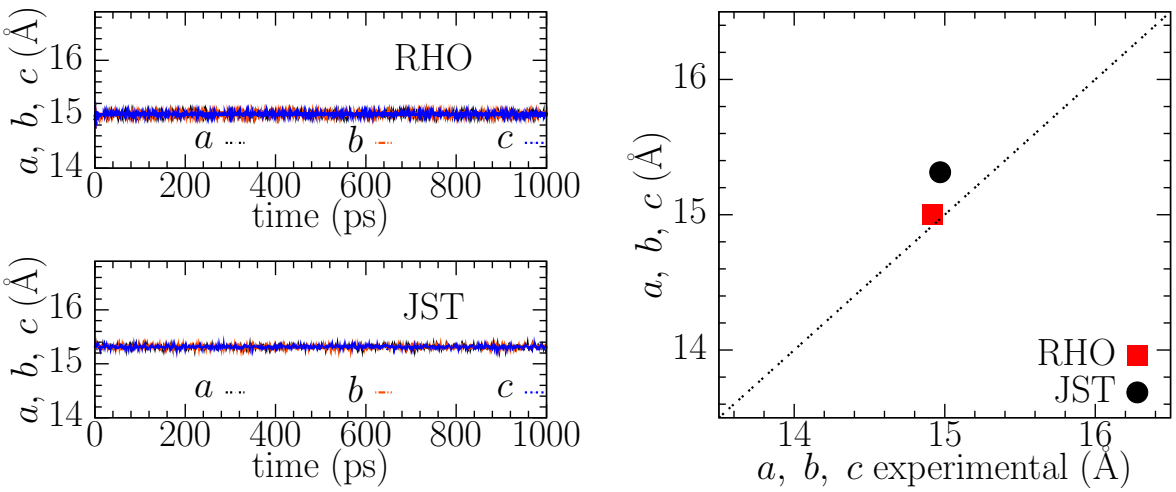

Figure 2: Time evolution as observed in molecular dynamics for the lattice parameters (a, b, and c) for RHO and JST zeolites. The right figure compares the crystallographic parameters a, b, c obtained using NσT molecular dynamics simulations using a Parrinello-Rahman barostat (y axis) and their experimental counterpart (x axis).[51]

3. Results

3.1 Acoustic and Mechanical Properties

3.1.1 Statistical physics route

Dynamic structure factor. The dynamic structure factor $S(\mathbf{q},\omega)$ is a key quantity which describes the complete structure and dynamics of a given system. In particular, as explained hereafter,the dynamic structure factor corresponds to the time and space Fourier transform of the Van Hove function $G(\mathbf{r},t)$ which describes the probability that two molecules i and j are separated by a vector $\mathbf{r}$ at time $t = 0$ and a time t, i.e. $\mathbf{r} = \mathbf{r}_i(t) - \mathbf{r}_j(0)$. In the context of the present work, $S(\mathbf{q},\omega)$ is a very important quantity as it includes all vibrational modes in the zeolite materials – including the low frequency (small ω) which corresponds to the propagation of a mechanical pressure wave through the solid (speed of sound). As discussed in what follows, considering this low frequency mode with wave vectors $\mathbf{q}$ chosen in the longitudinal mode or transverse mode provides a means to estimate the longitudinal and transverse sound velocities, respectively. These speeds of sound correspond

to the propagation of a sound wave which induces the following atomic displacement in the zeolite: $\delta x(t) \sim \cos[\omega_{\mathrm{L}}(q)t - qx]$ for a longitudinal wave and $\delta y(t) \sim \cos[\omega_{\mathrm{T}}(q)t - qx]$ for a transverse wave. With this example, in both cases, the sound wave propagates in the x direction and the induced displacement is along the same direction for a longitudinal wave and perpendicular to the propagation direction for a transverse wave. Moreover, while these two propagation modes lead to similar atom displacement equations, they propagate at different speeds to sound $v_{\mathrm{L}} = \lim_{q\to 0} \omega_{\mathrm{L}}/q$ and $v_{\mathrm{T}} = \lim_{q\to 0} \omega_{\mathrm{T}}/q$. Finally, as discussed in the next section, these speeds of sound can also be inferred from the elastic constants that describe the mechanical behavior of the material. This is due to the fact that an acoustic wave corresponds to the transmission of a mechanical pressure wave through the atoms so that this phenomenon and the related speed of sound is mechanical in nature.

Let us now introduce in detail the dynamic structure factor $S(\mathbf{q}, \omega)$ which is a cornerstone in molecular dynamics simulations and neutron scattering experiments to study the dynamical properties of solids, liquids and gases. For a solid phase, $S(\mathbf{q}, \omega)$ provides the phonon spectrum from molecular displacement and velocity field data. In particular, as shown later in this section, by looking at the low-frequency range ω, one can extract the speed of sound by fitting $S(\mathbf{q}, \omega)$ against a damped harmonic oscillator model.[56] Let us consider the density distribution at a position $\mathbf{r}$ and time t for a set of N particles: $\rho(\mathbf{r}, t) = \sum_{i=1}^{N} \delta[\mathbf{r} - \mathbf{r}_i(t)]$. The corresponding intermediate coherent scattering function $F(\mathbf{q}, t)$ – which is defined as the spatial Fourier transform of the Van Hove correlation function $G(\mathbf{r}, t)$ – writes:

$$F(\mathbf{q}, t) = \int G(\mathbf{r}, t)\ \exp(-i\mathbf{q}\cdot\mathbf{r})\mathrm{d}\mathbf{r} = \frac{1}{N}\left\langle \rho_{\mathbf{q}}(t)\rho_{-\mathbf{q}}(0)\right\rangle, \tag{1}$$

where $\rho_{\mathbf{q}}(t) = \int \rho(\mathbf{r}, t)\exp(-i\mathbf{q}\cdot\mathbf{r})\mathrm{d}\mathbf{r} = \sum_{i=1}^{N} \exp[-i\mathbf{q}\cdot\mathbf{r}_i(t)]$ are the Fourier components of the density distribution at time t (the second equality is obtained by inserting the sum of Dirac functions in the integral defined in the first equality). In turn, the dynamic structure factor is defined as the time Fourier transform of the intermediate coherent scattering

function:

$$S(\mathbf{q},\omega) = \frac{1}{2\pi}\int_{-\infty}^{+\infty} F(\mathbf{q},t)e^{i\omega t}\mathrm{d}t. \tag{2}$$

As shown in Appendix A, the dynamic structure factor can be related to the Fourier components of the particle flux $\mathbf{j}_\mathbf{q}(t) = \sum_{i=1}^{N} \mathbf{u}_i(t)\exp[-i\mathbf{q}\cdot\mathbf{r}_i(t)]$ where $\mathbf{u}_i(t)$ is the velocity of particle i at time t:

$$S_a(\mathbf{q},\omega) = \frac{1}{2\pi N}\left(\frac{q}{\omega}\right)^2 \int_{-\infty}^{+\infty} \left\langle j^a_\mathbf{q}(t) j^a_{-\mathbf{q}}(0)\right\rangle e^{i\omega t}\mathrm{d}t. \tag{3}$$

Here, $\mathbf{q}$ represents the wave vector, q is its norm, and a corresponds either to the longitudinal L or transverse T mode of the momentum current $j^a_\mathbf{q}(t)$.

In the present work, Eq. (3) was used to estimate $S(\mathbf{q},\omega)$ from the Fourier transform of the momentum current time correlation function. To assess the low frequency/small wave vector range in each direction of space (which allows deriving the macroscopic acoustic properties of the system as discussed hereafter), elongated zeolite supercells with a box size corresponding to $9\times3\times3$ unit cells were employed. Fig. 3 shows the longitudinal, $S_\mathrm{L}(\mathbf{q},\omega)$, and transverse, $S_\mathrm{T}(\mathbf{q},\omega)$, dynamic structure factors for a wave vector $\mathbf{q}\cdot\mathbf{e}_1 = 0.046$ Å^{-1} along the 100 symmetry axis (both data for RHO and JST zeolites are shown).

Sound velocities. The low-frequency peaks for the longitudinal mode in the dynamic structure factor were found at 0.0040 and 0.0024 rad/fs for the RHO and JST zeolites, respectively. On the other hand, the transverse mode peaks at low frequencies were found at 0.0024 and 0.0019 rad/fs, respectively. The wave vector dependence of the low-frequency peak observed in the dynamic structure factors was determined to estimate the speed of sound. In more detail, we consider the macroscopic limit ($q \to 0$) of the acoustic mode illustrated in Fig. 3 by fitting the Brillouin peak to a simple damped harmonic oscillator.[57]

$$S_a(\mathbf{q},\omega) \sim \frac{\Gamma_\mathrm{a}(\mathbf{q})\omega^2_\mathrm{a}(\mathbf{q})}{[\omega^2_\mathrm{a}(\mathbf{q}) - \omega^2]^2 + \omega^2\Gamma^2_\mathrm{a}(\mathbf{q})}. \tag{4}$$

The low-frequency peaks obtained from the dynamic structure calculations are fitted with

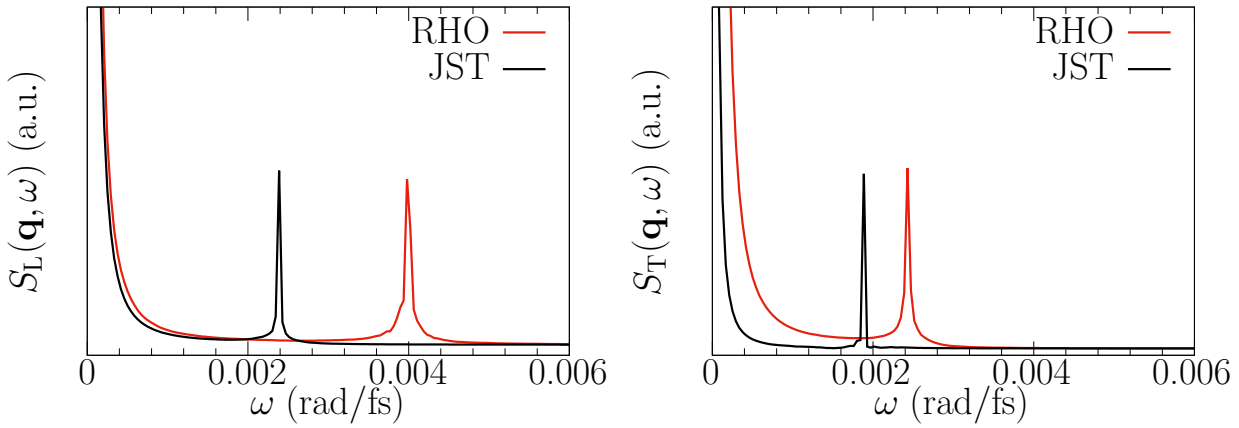

Figure 3: Longitudinal $S_{\rm L}(\mathbf{q},\omega)$ and transverse $S_{\rm T}(\mathbf{q},\omega)$ dynamic structure factors as a function of wave vector $\mathbf{q}\cdot\mathbf{e}_1 = 0.046$ Å^{-1} in the (100) direction. The angular frequency $\omega_{\rm a}$ (rad/fs) and corresponding speed of sound $v_{\rm a}$ is obtained by fitting the observed peak to a damped harmonic oscillator model as explained in the text. The low frequency peaks for the longitudinal mode are found at 0.0040 and 0.0024 rad/fs and for transverse mode at 0.0024 and 0.0019 rad/fs for RHO and JST zeolites, respectively.

parameters $\omega_{\rm a}$ (used for the estimation of sound velocities, $v_{\rm a} = \omega_{\rm a}/q$) and $\Gamma_{\rm a}$ (broadening). Fig. 4 shows the wave-vector dependence of the longitudinal $v_{\rm L}$ and transverse $v_{\rm T}$ sound velocities along the (100) direction. The sound velocity increases with a decrease in $q = |\mathbf{q}|$ and reaches a constant as the wave vector approaches the macroscopic limit ($q \to 0$) of the speeds of sound. We also determined the acoustic velocities in the (110) and (111) directions, leading to the results shown in Table 3. In all directions of wave propagation considered in our study, the longitudinal and transverse modes of acoustic velocities are higher in RHO zeolites compared to the JST zeolite systems. In the limit $q \to 0$, as will be discussed below in the section dealing with the mechanical section, we know that $v_{\rm L} \sim \sqrt{C_{11}/\rho}$ while $v_{\rm T} \sim \sqrt{C_{44}/\rho}$ where C_{11} and C_{44} are the elastic components of the stiffness tensor. Therefore, the large difference in $v_{\rm L}$ and small difference in $v_{\rm T}$ between the two zeolites is due to intrinsic differences in the elastic parameters (since the two solids have similar mass densities). Differences in the elastic constants but also in the related bulk, Young, and shear moduli are due to different topologies in the silica framework. As for the differences observed between the two zeolites in the q dependence of the longitudinal and transverse modes, one

should consider the complex phonon structure in such materials which possess many atoms per unit cell. In this case, the solution at a non-zero wavevector reflects the rich vibrational spectrum of the material which depends on the exact molecular arrangement of the atoms in the unit cell. As a result, while the two zeolite samples share common features such as a cubic structure, an all-silica chemical composition, and similar densities, the topology in these samples can lead to different vibrational properties.

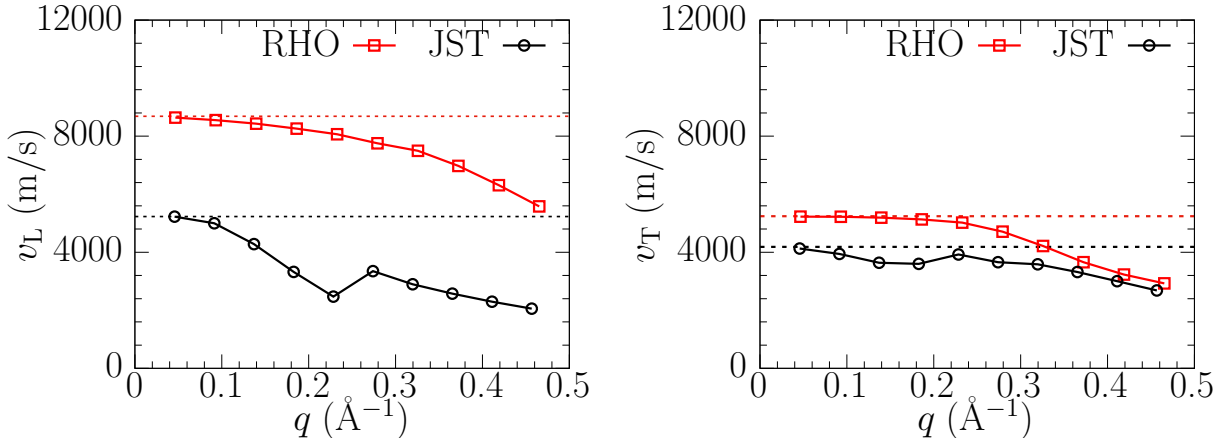

Figure 4: Longitudinal v_L and transverse v_T velocity for RHO and JST zeolites as a function of the wave vector in the (100) direction (note that for this specific direction, the two transverse modes are identical). The horizontal dashed line represents the macroscopic limit of the speeds of sound as obtained from the macroscopic route discussed in the mechanical route section (derived from mechanical constants obtained using either the direct or fluctuation approaches).

3.1.2 Mechanical route

Acoustic wave propagation can be assessed by probing the mechanical behavior of a given material. From a general viewpoint, in the limit of small mechanical deformations (elastic regime), the mechanical behavior of a material can be characterized by introducing the stress σ and strain ϵ. In a solid medium, the strain at a given position cannot be described by a single vector only since the same element of volume can be compressed, stretched and sheared. Similarly, the stress at a given position cannot be discussed by a single force as the same stress can correspond to pushing, pulling, and shearing at once. Therefore, both the

stress σ and strain σ at a given point need to be defined as second-rank tensors which can be written as 3×3 matrices whose elements are σ_{ij} and ϵ_{ij} with i, j, k, and l are x, y, or z. Upon small, i.e. elastic, deformations, the stress and strain are assumed to be proportional which can be seen as a generalized Hooke's law: $\sigma_{ij} = C_{ijkl}\epsilon_{kl}$ where C_{ijkl} is the stiffness tensor. As discussed below, the stiffness matrix is essential as it describes the mechanical response to compression, dilation, and shearing. In particular, combination of the C_{ijkl} allows estimating the bulk modulus K (resistance to bulk compression), the shear modulus G (resistance to shearing), the Young modulus E (resistance to a linear compression), and Poisson ratio ν (ratio of the deformation in a given direction when straining in another direction). Moreover, in the context of the present study, the coefficients C_{ijkl} allows estimating the longitudinal v_L and transverse v_T speeds of sound in a given material.

The coefficients of the fourth-rank elasticity tensor $\mathbf{C}$ are fundamental parameters that describe the mechanical properties of materials. In turn, these parameters can be used to study the acoustic properties of a solid structure as illustrated here. For cubic materials, like RHO and JST zeolites considered in our study, only 3 elastic constants, C_{11}, C_{12} and C_{44}, are required to describe their mechanical behavior. Using Voigt compact notation, the elasticity matrix corresponding to a material having cubic symmetry is represented as:

$$\mathbf{C} = \begin{bmatrix} C_{11} & C_{12} & C_{12} & 0 & 0 & 0 \\ & C_{11} & C_{12} & 0 & 0 & 0 \\ & & C_{11} & 0 & 0 & 0 \\ & & & C_{44} & 0 & 0 \\ & symm. & & & C_{44} & 0 \\ & & & & & C_{44} \end{bmatrix} \tag{5}$$

In the present study, we followed two different approaches to measure the mechanical constants involved in the above matrix: a strain-fluctuation approach and a more direct mechanical test. Then, the acoustic properties of the two materials under study were inferred

using these macroscopic mechanical constants.

Strain fluctuation approach. A method for determining temperature-dependent elastic constants of a material using MD simulations is from the fluctuations in the strain in the system at thermal equilibrium without applying any external force. This strain fluctuation approach, which was derived by Parrinello and Rahman,[49] is based on the spontaneous fluctuations observed in the system's dimensions. As shown in Appendix B, the fundamental equation used in the strain fluctuation method is given by:

$$< \epsilon_{ij}\epsilon_{kl} > - < \epsilon_{ij} >< \epsilon_{kl} >= \frac{k_B T}{\Omega_0} S_{ijkl}, \tag{6}$$

where k_B is Boltzmann constant, Ω_0 is the volume of the system and S_{ijkl} is the elastic compliance tensor (the inverse of the elastic stiffness tensor), and $\langle\ \rangle$ denotes the ensemble average in a constant particle number, stress, and temperature ($N\sigma T$) ensemble. Using Eq. (6) is convenient as the strain tensor can be written in terms of the fluctuations in the h matrix, which corresponds to the instantaneous dimensions of the simulation box with respect to the reference system h_0 (the latter is obtained as the equilibrium value by averaging over a sufficiently large set of molecular configurations). The elastic constants are thus derived from the instantaneous length and angles of the edges of the simulation box. In more detail, the instantaneous strain tensor ϵ and the h matrix are related by Eq. (7):[58]

$$< \epsilon_{ij} >= \frac{1}{2}\left[((h_0^{-1})^T h^T h h_o^{-1})_{ij} - \delta_{ij}\right]. \tag{7}$$

The transpose of the given h matrix is indicated by the superscript T. In practice, we performed MD simulations to calculate the instantaneous values of the length and angles of the simulation box by allowing the volume and shape of the supercell to change over time.

To predict elastic constants using the strain-fluctuation approach, the zeolite supercells were monitored for 8 ns to assess the strain-correlation function $< \epsilon_{ij}\epsilon_{kl} >$. In the long time limit, the running averages of the strain-correlations reach steady values for the estimation

of elastic constants. Fig. 5 shows the time evolution of $< \epsilon_{ij}\epsilon_{kl} >$ (with $i, j, k, l = x$, y or z) for the two zeolite structures RHO and JST. The strain-correlations $< \epsilon_{11}\epsilon_{11} >$, $< \epsilon_{11}\epsilon_{22} >$ and $< \epsilon_{23}\epsilon_{23} >$ are used to determine the three independent elastic constants C_{11}, C_{12} and C_{44} for RHO and JST zeolite structures using Eq. (6). The elasticity matrix C_{ijkl} are obtained by taking the inverse of the compliance matrix $C_{ijkl} = (S_{ijkl})^{-1}$ calculated using Eq. (6). The values of C_{11}, C_{12} and C_{44} are 98.68, 68.15 and 38.74 GPa for RHO zeolite and the corresponding values for JST zeolite are 36.32, -7.82 and 23.76 GPa, respectively. The positive strain-correlation $< \epsilon_{11}\epsilon_{22} >$ for JST zeolite is indicative of the auxetic properties which is confirmed by the negative value of C_{12}. The elasticity matrix of RHO and JST zeolites are found to obey the necessary and sufficient elastic stability conditions (C_{11} - C_{12} > 0; $C_{11} + 2C_{12} > 0$; $C_{44} > 0$) for the cubic system.[59]

Using the elastic parameters C_{ij}, we determined a single, representative Young's modulus E, shear modulus G, bulk modulus K, Poisson's ratio ν and Zener ratio A for RHO and JST zeolites as follows:[60]

$$K = \frac{C_{11} + 2C_{12}}{3};\ G = C_{44};\ E = \frac{C_{11}^2 + C_{11}C_{12} - 2C_{12}^2}{C_{11} + C_{12}};$$
$$\nu = \frac{C_{12}}{C_{11} + C_{12}};\ A = \frac{2C_{44}}{C_{11} - C_{12}}. \tag{8}$$

The material properties for RHO and JST zeolites calculated from the elastic constants obtained by the strain-fluctuation approach are shown in Table 2. A low bulk modulus for JST zeolite suggests the material to be largely compressible under pressure when compared to the RHO zeolite. Siddorn `et al.`[55] reported the 3 independent elastic constants of JST zeolite calculated using different force fields. All force fields used in the study[55] predicted auxetic properties for the JST zeolite. The force field proposed by Ghysels `et al.`[53] used in the present study also predicts a negative Poisson's ratio. The Zener ratio A, a measure

of the anisotropy of elastic behavior in cubic crystals, is found to be 1.08 for JST zeolite indicating the quasi-isotropic behavior of the material, whereas RHO zeolite with $A = 2.54$ shows a stronger anisotropy.

Table 2 also shows the values obtained for many parameters such as mechanical moduli, lattice parameter, and Zener and Poisson ratios as obtained using previous DFT calculations.[55,61] While the difference between the values obtained in this work and those obtained from DFT calculations is non-negligible, such departure should be considered in detail considering the following points. First, upon considering similar zeolites with cubic structures, large differences are observed in their bulk modulus with values ranging from ~ 3 to ~ 130 GPa. To illustrate this aspect, Fig. S1 in the Supporting Information shows that the bulk modulus and density in cubic zeolites are not strongly correlated despite large variations in both quantities. As already mentioned, this points to the role of the molecular arrangement, i.e. molecular topology, of the Si and O atoms in the unit cell of these crystalline structures. This result is supported by the work by Poloni and Kim[61] who observed correlations upon plotting the dielectric constant of zeolites against their density but no strong correlations against their bulk modulus (in fact, as expected, the bulk modulus tends to increase with density but the correlation is not marked as significant scattering of the data is observed). As a result, the difference between the bulk moduli obtained using classical and quantum calculations – without being negligible – can be judged as acceptable considering that the predicted values fall within the appropriate regions of low and high bulk moduli. Second, as shown by Siddorn et al.,[55] it is interesting to note that different classical force fields lead to elastic constants that vary around the experimental or DFT calculated values. Typically, Fig. 6 in Ref.[55] shows that (1) C_{11} varies from 15.4 GPa to 36.5 GPa (compared to 29.41 using DFT), (2) C_{12} varies from -13.1 GPa to -5.7 GPa (compared to -8.4 using DFT), and (3) C_{44} varies from 13.1 GPa to 21.4 GPa (compared to 18.2 using DFT). As a result, while the absolute difference between the bulk modulus predicted using classical and quantum calculations is of the order of 2-3 GPa, the empirical force field used in the present work

is assumed to provide a reasonable picture when considering zeolite materials with very different mechanical properties (RHO versus JST).

Table 2: Mechanical parameters of RHO and JST zeolites as obtained from strain-fluctuation approach using MD simulations. All units are in GPa except for the Poisson's and Zener's ratios which are dimensionless and the lattice parameter in Å units. The structural and mechanical properties calculated from DFT (ab initio) calculations[55,61] are shown in parentheses.

Material	a	E	G	K	ν	A
RHO	15.00 (15.15)	43.01	38.74	78.33 (75.6)	0.408	2.54
JST	15.30 (15.38)	32.17 (22.7)	23.77 (18.2)	6.89 (4.2)	-0.274 (-0.39)	1.08 (1.04)

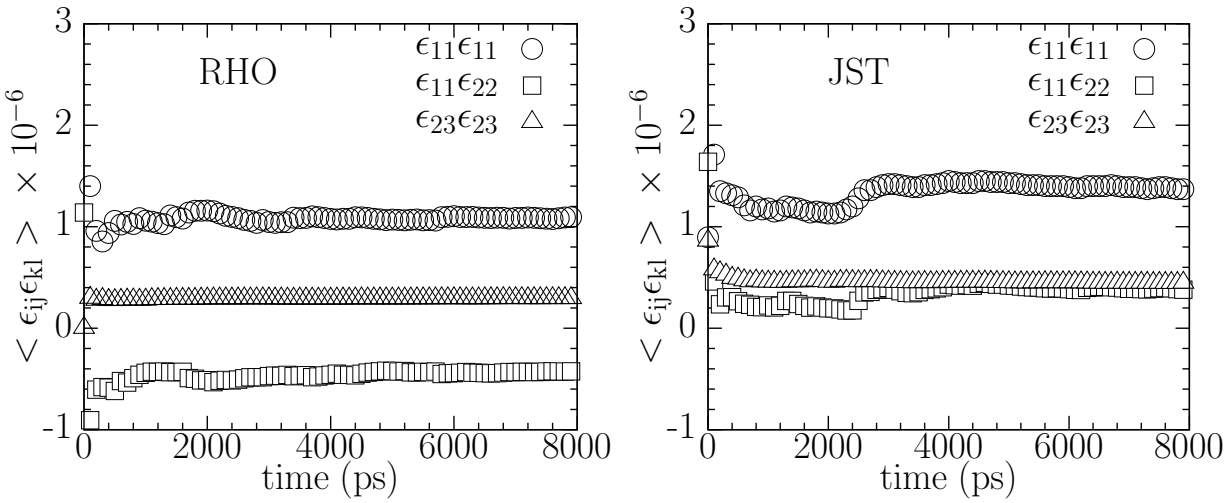

Figure 5: Time evolution of strain correlation $< \epsilon_{ij}\epsilon_{kl} >$ (with $i, j, k, l = x$, y or z) for RHO and JST zeolites. As discussed in the text, the elastic constants C_{11}, C_{12} and C_{44} can be inferred from the strain correlation $\epsilon_{11}\epsilon_{11}$, $\epsilon_{11}\epsilon_{22}$, $\epsilon_{23}\epsilon_{23}$.

Mechanical test. Using MD simulations, RHO and JST zeolites were subjected to tensile and shear deformations by applying a constant strain rate of 1.0×10^{-6} s^{-1}. In MD, the macroscopic stress developed while inducing tensile or shear strain to a solid material is calculated by taking into account the energy contribution from particle motion as well as virial stress. The components of the macroscopic stress tensor σ_{ij} in volume V can therefore be evaluated using:

$$\sigma_{\mathrm{ij}} = \frac{1}{V}\left(-\sum_{a\in V} m^{(a)} v_{\mathrm{i}}^{(a)} v_{\mathrm{j}}^{(a)} - W_{\mathrm{ij}}\right), \tag{9}$$

where $v_{\mathrm{i}}^{(a)}$ and $v_{\mathrm{j}}^{(a)}$ are the ith and jth component velocities of particle a having mass m. The virial contribution W_{ij} due to intramolecular and intermolecular interactions can be expressed as:

$$W_{\mathrm{ij}} = -\frac{1}{2}\sum_{a\in V}\sum_{b\in V}((r_{\mathrm{i}}^{(a)} - r_{\mathrm{i}}^{(b)})F_{\mathrm{j}}^{(ab)}) \ , \tag{10}$$

where $F_{\mathrm{j}}^{(ab)}$ is the total force exerted by particle b on a along the j-th vector component (the particles a and b are separated by a distance $r_{\mathrm{i}}^{(a)} - r_{\mathrm{i}}^{(b)}$ along the i-th vector component).

The tensile test, shown in Fig. 6 a), is carried out by deforming the RHO and JST zeolites along the x-direction with the tensile strain defined by $\epsilon_{\mathrm{x}} = \Delta L/L_0$. To apply shear, the top surface of the zeolites is displaced along the x-direction while keeping the bottom surface fixed in position, as shown in Fig. 6 b). The total shear deformation applied to the zeolite structure can be evaluated in terms of the engineering shear strain $\gamma_{\mathrm{xy}} = \Delta L/L_0$.

In Fig. 7, the components of the stress tensor produced – calculated using Eq. (9) – as a result of the deformation induced in zeolites are plotted as a function of the developing strain. The 3 independent elastic constants for RHO and JST zeolite structures are derived by fitting the linear elastic regime of the stress-strain ($\boldsymbol{\sigma}$ vs $\boldsymbol{\epsilon}$) curve. A linear fit to the $\boldsymbol{\sigma}$ vs $\boldsymbol{\epsilon}$ curve is confirmed by considering approximately 10% of the strain applied for the mechanical failure of the material. From the tensile test, the ratio of the stress components σ_{x} and σ_{y} to the tensile strain applied along the x-direction (ϵ_{x}) yields material constants C_{11} and C_{12}; the corresponding values are 106.81 and 71.96 GPa for RHO zeolite and 36.46

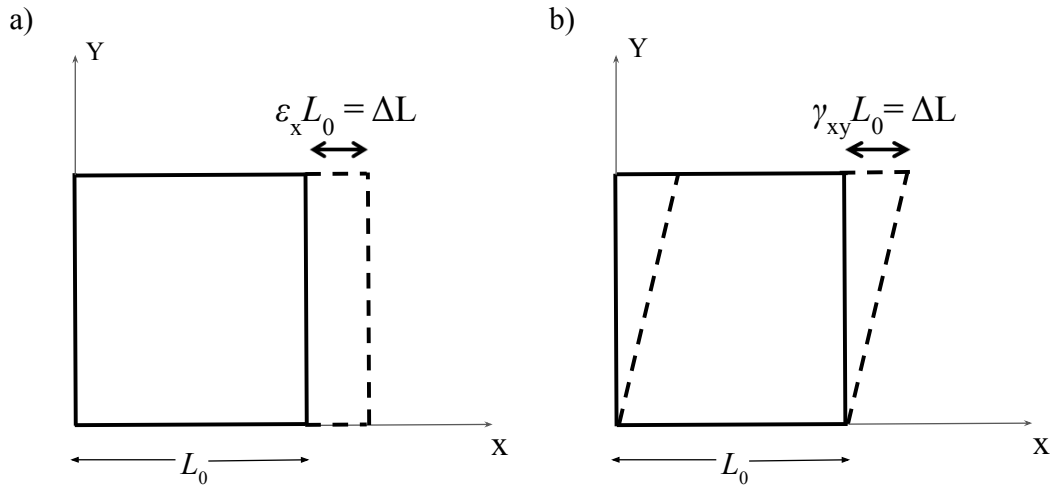

Figure 6: Schematic of the uniaxial tensile (a) and shear (b) tests performed on zeolite super cells using MD simulations. The undeformed configuration of the zeolite is represented by continuous lines while the deformed configuration after tensile and shear tests is shown by dashed lines. L_0 is the length of the undeformed system. a) For the tensile test, the 3D zeolite structure is deformed along x-direction. The tensile strain ϵ_x is defined as the ratio of total change in length due to tensile deformation ΔL to the initial length of the super cell L_0. b) To apply shear, the top of the zeolite (yz plane) is deformed along x-direction while keeping the bottom fixed in position. The shear strain γ_{xy} is defined as the ratio between the amount of deformation and the length perpendicular to the surface in which the deformation is applied.

and -8.43 GPa for JST zeolite. The elastic constant C_{44} – which is equivalent to the shear modulus G of the material – is calculated from the stress τ_{xy} developed upon shearing the supercell in the x-direction while keeping the lower surface of zeolite fixed in position. The value of C_{44} for RHO zeolite obtained from the shear test using MD is 38.86 GPa and 23.36 GPa for JST zeolite. To verify the validity of our results, considering the cubic symmetry of the material under study, it is checked that tensile tests in y and z-directions and shear tests on xy and zx planes yield the same values. From the tensile tests we found $C_{11} = C_{22} = C_{33}$ and $C_{12} = C_{13} = C_{23}$ and the elastic constants C_{55} and C_{66} calculated from the shear tests to be the same as C_{44} with an error of less than 2%.

The two following matrices correspond to the elasticity matrix in Voigt notation for the RHO and JST zeolites, respectively. The values in parentheses indicate the elastic constants obtained from the strain-fluctuation approach. All the stiffness values reported here are evaluated in GPa.

$$\mathbf{C}_{\mathrm{RHO}} = \begin{bmatrix} 106.81\ (98.68) & 71.96\ (68.15) & 71.96\ (68.15) & 0 & 0 & 0 \\ & 106.81\ (98.68) & 71.96\ (68.15) & 0 & 0 & 0 \\ & & 106.81\ (98.68) & 0 & 0 & 0 \\ & & & 38.86\ (38.74) & 0 & 0 \\ & \textit{symm.} & & & 38.86\ (38.74) & 0 \\ & & & & & 38.86\ (38.74) \end{bmatrix}$$

$$\mathbf{C}_{\mathrm{JST}} = \begin{bmatrix} 36.46\ (36.32) & -8.43\ (-7.82) & -8.43\ (-7.82) & 0 & 0 & 0 \\ & 36.46\ (36.32) & -8.43\ (-7.82) & 0 & 0 & 0 \\ & & 36.46\ (36.32) & 0 & 0 & 0 \\ & & & 23.36\ (23.76) & 0 & 0 \\ & \textit{symm.} & & & 23.36\ (23.76) & 0 \\ & & & & & 23.36\ (23.76) \end{bmatrix}$$

Sound velocities. Using the elasticity tensor $\mathbf{C}$, the longitudinal and transverse modes of sound propagation in zeolites are predicted from the solution of the Kelvin-Christoffel's equation:

$$[\Gamma_{\mathrm{ik}} - \rho v^2 \delta_{\mathrm{ik}}] p_{\mathrm{k}} = 0, \tag{11}$$

where the Christoffel's tensor $\Gamma_{\mathrm{ik}} = C_{ijkl} n_{\mathrm{j}} n_{\mathrm{l}}$ is related to the stiffness tensor and the unit

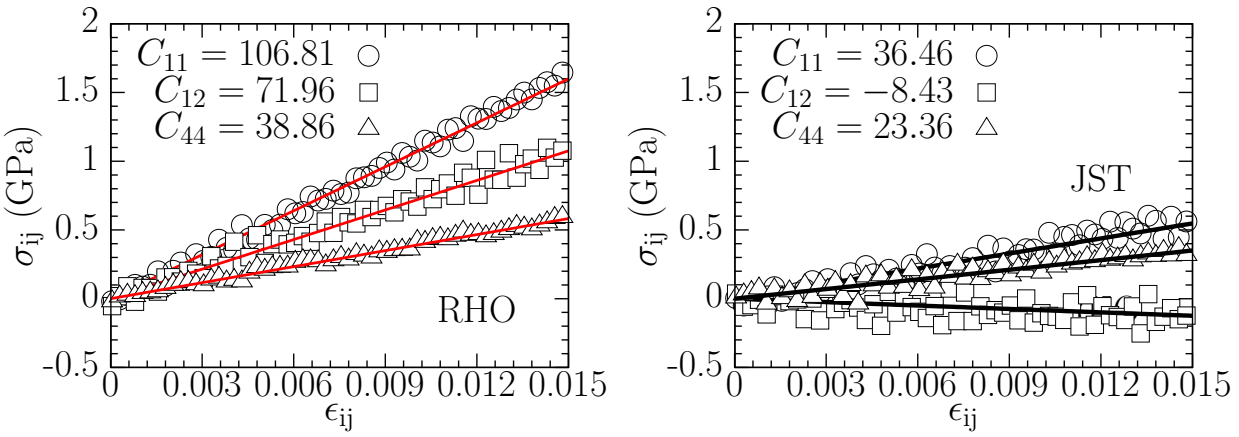

Figure 7: Stress-strain curves $\sigma_{ij}/\epsilon_{ij}$ for RHO and JST zeolites determined from the mechanical tests using MD simulations. A uniaxial tensile test is performed to derive elastic constants C_{11} and C_{12} while C_{44} is calculated by conducting a shear test on the zeolite structure. A linear fit to the stress-strain curve, which corresponds to the red and black lines for RHO and JST zeolites, yield the respective elastic constant. The elastic constants C_{11}, C_{12} and C_{44} for RHO and JST zeolites obtained from the mechanical tests are shown in GPa units.

slowness vector **n** (i.e. the direction of wave propagation). $p_{\rm k}$ represents the polarization vector, v the sound velocity and ρ the mass density of the material. As indicated by Eq. (11), the determination of wave motion is an eigenvalue problem. Due to the elasticity tensor symmetry, $\Gamma_{\rm ik} - \rho v^2 \delta_{\rm ik}$ is also symmetrical so that the resulting three eigenvalues on solving Eq (11) are real. We estimated the longitudinal ($v_{\rm L}$) and transverse ($v_{\rm T1}$ and $v_{\rm T2}$) speeds of sound along axes (100), (110) and (111) for RHO and JST zeolite structures by solving Eq. 11. For example, the acoustic velocity in the (100) direction is $v_{\rm L} = \sqrt{C_{11}/\rho}$ along the longitudinal direction and $v_{\rm T1}$, $v_{\rm T2} = \sqrt{C_{44}/\rho}$ along the transverse directions. The density ρ for RHO and JST zeolites are 1417 and 1334 kg/m^3, respectively.

The speeds of sound averaged over 5 simulations with different initial configurations together with the standard error are shown in Table 3. As can be seen, the acoustic velocities obtained using the strain fluctuation method and mechanical tests in different propagation directions are in good agreement with the sound velocities predicted using the dynamic structure factor. The higher sound velocities for the RHO zeolite (in all propagation directions) arise from its higher stiffness when compared to the elastic constants for the JST structure.

The longitudinal or transverse modes of acoustic velocities in RHO zeolite are different along the three different axes of symmetry (Table 3). This is consistent with the results of elastic constants obtained from the mechanical route where RHO zeolite is found to be not perfectly isotropic. For a completely isotropic material, the Zener ratio must be equal to one.[62] For RHO zeolite, this criterion is not satisfied as $A = 2.54$; the weak anisotropy in RHO zeolite thus leads to the orientation-dependent acoustic velocity. On the other hand, the acoustic velocities in JST zeolite along (100), (110) and (111) directions are almost identical which is consistent with the fact that the Zener ratio approximately equals to 1 ($A = 1.08$).

Table 3: Longitudinal [v_{L}] and transverse [v_{T1} and v_{T2}] speeds of sound in RHO and JST zeolites for different wave propagation directions. The speeds of sound are in m/s. The standard error on the averaged values of longitudinal and transverse speeds of sound for RHO and JST zeolites are also shown in the table. The velocity data predicted from the dynamic structure factor method are obtained by utilizing elongated zeolite systems.

RHO	100			110			111		
Speed of sound (m/s)	$S(\mathbf{q},\omega)$	Direct	Fluctuation	$S(\mathbf{q},\omega)$	Direct	Fluctuation	$S(\mathbf{q},\omega)$	Direct	Fluctuation
v_{L}	8640	8682 (±9)	8345 (±27)	9228	9513 (±8)	9285 (±21)	9246	9775 (±7)	9577 (±19)
v_{T1}	5225	5236 (±1)	5228 (±3)	3436	3506 (±1)	3282 (±15)	4105	4164 (±1)	4036 (±8)
v_{T2}	5225	5236 (±1)	5228 (±3)	4710	5236 (±1)	5228 (±3)	4105	4164 (±1)	4036 (±8)

JST	100			110			111		
Speed of sound (m/s)	$S(\mathbf{q},\omega)$	Direct	Fluctuation	$S(\mathbf{q},\omega)$	Direct	Fluctuation	$S(\mathbf{q},\omega)$	Direct	Fluctuation
v_{L}	5232	5226 (±3)	5216 (±24)	5378	5291 (±3)	5337 (±25)	5468	5312 (±3)	5376 (±26)
v_{T1}	4164	4182 (±2)	4219 (±14)	3903	4100 (±1)	4066 (±12)	3846	4128 (±1)	4118 (±11)
v_{T2}	4033	4182 (±2)	4219 (±14)	3643	4182 (±2)	4219 (±14)	3833	4128 (±1)	4118 (±11)

3.2 Upscaling approach

This section makes use of the results of the molecular simulations and an upscaling method to investigate the effective mechanical and acoustic properties of empty double porosity materials formed by adding an extra scale of porosity to a nanoporous zeolite-made skeleton. Such extra scale of porosity can be a result of the materials' manufacturing process or purposely introduced, and can represent larger pores, voids in between consolidated nanoporous grains, and/or possible large defects or microfractures in the nanoporous skeleton, among others. The effects of these local heterogeneities, which will be referred simply as pores, can be probed by acoustic waves, as it will be shown below.

To derive the macroscopic equation that determines the macroscopic displacement of the double porosity material, an upscaling method called the two-scale asymptotic method of homogenization[50] is used. This method will be referred to, for short, as homogenization.

Homogenization is a mathematical method that enables the derivation of macroscopic models starting from the mathematical description of physical phenomena occurring at a local scale determined by a characteristic size or period of the material ℓ. The method relies on the concept of separation of scales (i.e. $\ell/\lambda \ll 1$ in acoustics) and provide a description of a heterogeneous medium as an equivalent continuum with effective parameters that account for the influence of the local physics on the medium's macroscopic properties. Thus, homogenization allows linking the large-scale observable behavior with local mechanisms governed by a set of equations formulated at the local scale. Key advantages of homogenization are that it rigorously provides macroscopic models, gives a recipe for the calculation of the effective parameters, sheds light on the physical origin of the macroscopic behavior, and indicates the validity domain of the upscaled model.

The used upscaled method consists in the following steps: i) Formulation of the physics at the local scale and introduction of two dimensionless variables: one that accounts for local variations, another that describes macroscopic variations; ii) Physical analysis of the local governing equations to determine the relative order of magnitude of the terms in the

equations as well as whether the unknown variables fluctuate locally or macroscopically; iii) Nondimensionalization and rescaling of the local equations, iv) Insertion into the local equations of the unknown variables written in the form of asymptotic expansions of powers the small parameter $\epsilon = \ell/\lambda \ll 1$; v) Identification of boundary value problems by collecting terms with equal powers of ε and derivation of the macroscopic equations. It is noted that the effective parameters are calculated from the solution of the identified boundary value problems, as shown in the Appendix C where classical results[50] on the upscaling of the wave equation in porous solids are presented.

The studied periodic double porosity materials comprise a drained nanoporous skeleton Ω_s and empty pores Ω_f, as schematically shown in Figure 8. It is recalled that the period or local characteristic size of the material is ℓ and the macroscopic characteristic size L is related to the sound wavelength λ via $L = \lambda/2\pi$. The skeleton has a volume fraction $\varphi = \Omega_s/\Omega$ and its common boundary with Ω_f is Γ. The outward-pointing vector normal to Γ is $\mathbf{n}$. We shall note that the separation of scales is ensured, provided that ℓ is much larger than the nanoscopic characteristic size [*e.g.* $\ell = \mathcal{O}(1\ \mu m)$] and, at the same time, much smaller than the macroscopic characteristic size L, i.e. $\ell \ll L$. Moreover, i) only long-wavelength acoustic wave propagation through the solid part of the multiscale material is accounted for, and ii) the nanoporous skeleton is effectively isotropic due to the assumed random orientation of the zeolite crystals it is made of and/or its isotropic or quasi-isotropic behavior.

As derived in the Appendix C, the effective elasticity tensor $\mathbf{a}$ of the double porosity material is given by

$$a_{ijkh} = \varphi C_{ijkh} + C_{ijlm}\langle e_{lm}(\boldsymbol{\xi}^{kh})\rangle, \tag{12}$$

where $\mathbf{C}$ is the effective elasticity tensor of the skeleton (computed in previous sections), $\langle\cdot\rangle = \Omega^{-1}\int_{\Omega_s}\cdot d\Omega$ is the spatial mean operator, $\mathbf{e}_y(\cdot) = e_{lm}(\cdot)$ is the local strain tensor, and ξ_i^{kh} represents the i-th component of the microscopic skeleton displacement in response to a macroscopic strain excitation $\mathbf{E} = \frac{1}{2}(\mathbf{e}_k \otimes \mathbf{e}_h + \mathbf{e}_h \otimes \mathbf{e}_k)$. Note that ξ_i^{kh} is calculated from the

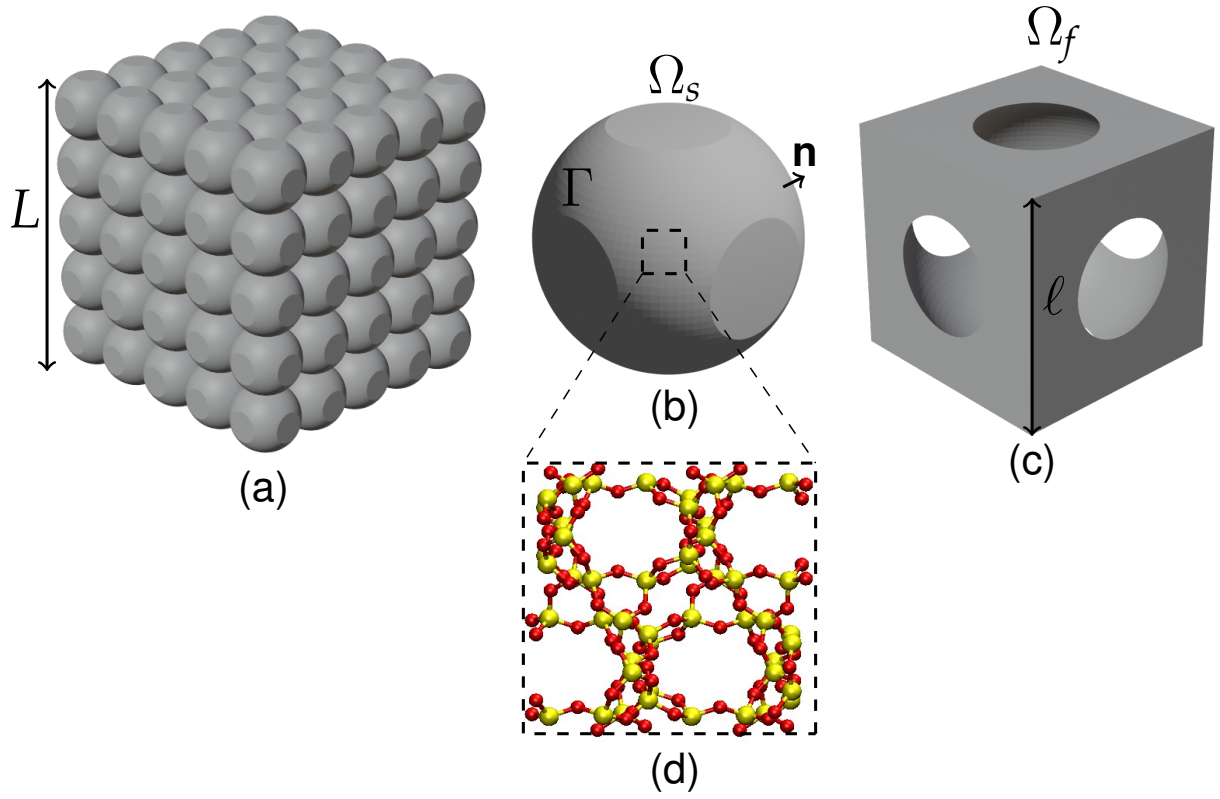

Figure 8: Periodic geometry of a double porosity material comprising a drained nanoporous skeleton and empty pores. (a) Macroscopic sample. (b) Nanoporous skeleton part Ω_s of the representative elementary volume (REV). (c) Empty pores Ω_f in the REV. (d) JST zeolite unit cell.

solution of the boundary value problem (42)–(43).

As an example, we consider in this work an array of overlapping spheres arranged in a simple cubic lattice[63,64] (see Figure 8). The spheres are made of the quasi-isotropic JST or RHO zeolites studied in previous sections. Owed to the cubic symmetry of the double porosity material microstructure, the effective elasticity tensor can be written as[64,65]

$$a_{ijkh} = \lambda_p \delta_{ij}\delta_{kh} + \mu_{1p}[\delta_{ik}\delta_{jh} + \delta_{ih}\delta_{jk}] + 2\mu_{2p}\delta_{ijkh} - 2\mu_{1p}\delta_{ijkh}, \tag{13}$$

where $\delta_{ijkh} = 1$ for $i = j = k = h$ or $\delta_{ijkh} = 0$ otherwise; and the effective parameters are the first Lamé parameter λ_p and two shear moduli, namely μ_{1p} and μ_{2p}, which characterize the shear resistance of the material in the planes $(\mathbf{e}_i, \mathbf{e}_k)$ and $(\mathbf{e}_i + \mathbf{e}_j, \mathbf{e}_k)$, respectively. By

matching Eqs. (12) and (13), the following link between the local strain components, elastic parameters and volume fraction of the skeleton, and effective elastic parameters of the double porosity material is found[64,65]

$$\frac{\lambda_p}{\lambda} = \varphi + f + 2g(1 + \frac{G}{\lambda}) \tag{14}$$

$$\frac{\mu_{2p}}{\mu} = \varphi + f - g \tag{15}$$

$$\frac{\mu_{1p}}{\mu} = \varphi + h, \tag{16}$$

where $f = \langle e_{11}(\xi^{11})\rangle$, $g = \langle e_{22}(\xi^{11})\rangle = \langle e_{33}(\xi^{11})\rangle$, $h = \langle e_{12}(\xi^{12})\rangle$, and ξ^{11} and ξ^{12} are solutions of Eqs. (42)–(43) for solicitations $E_{11} = 1$ and $E_{12} = 1$, respectively. It is noted that, in deriving these equations, the constitutive material of the solid skeleton has been assumed isotropic. This appears as a reasonable simplifying assumption not only because of the assumed random orientation of the JST or RHO crystals in the grains but also due to the Zener ratio of 1.08 for JST or 2.54 for RHO (see the respective discussion in preceding sections) which indicates their quasi-isotropic and weakly anisotropic nature, respectively. Moreover, it is recalled that the Lamé parameters of the skeleton, i.e. λ and μ, are related to Young's modulus E, Poisson's ratio ν, and bulk modulus K in a classical manner: $\lambda = E\nu/(1+\nu)(1-2\nu)$, $G = E/2(1+\nu)$, and $K = \lambda + 2\mu/3$. On the other hand, a unique effective Young's modulus and Poisson's ratio can be defined,[64] relative to the principal axes of the microstructure, as $E_p = 3\mu_{2p}(\lambda_p + 2\mu_{2p}/3)/(\lambda_p + \mu_{2p})$ and $\nu_p = \lambda_p/2(\mu_{2p} + \lambda_p)$, while the bulk modulus reads as $K_p = \lambda_p + 2\mu_{2p}/3$ (see also Eq. (8)).

Figure 9 shows the normalized effective parameters [i.e. λ_p/λ, μ_{1p}/G and μ_{2p}/G; and E_p/E, ν_p/ν and K_p/K] of the array of aggregated spheres made of JST or RHO zeolite as a function of the volume fraction. For the JST-based double porosity material, the normalized shear moduli increase as the volume fraction does. This is also the case for the normalized Young's and bulk moduli, as can be seen in Figure 9. Therefore, these parameters behave in a conventional way (cf. Fig. 9 and the results in[50,63,64]).

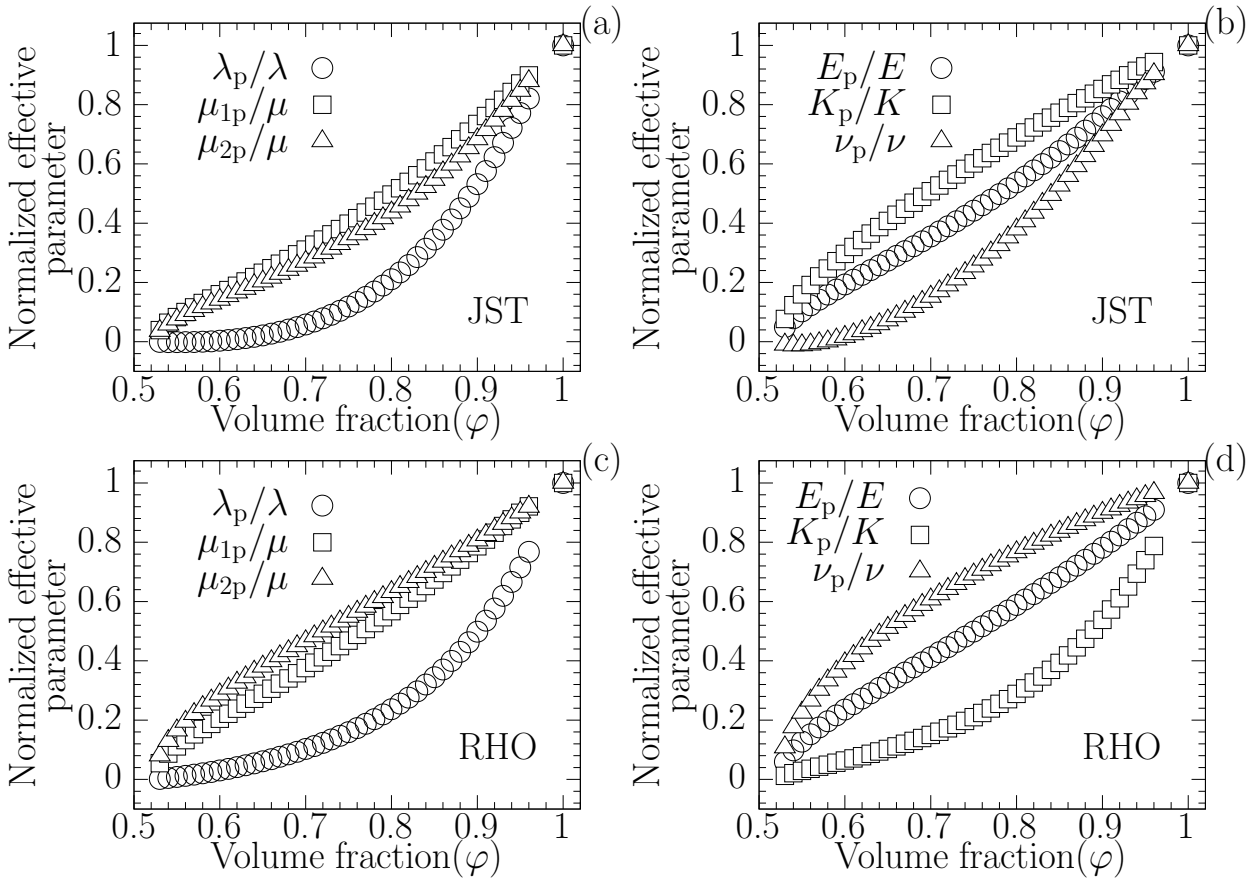

Figure 9: Normalized effective parameters, first Lamé parameter, shear moduli Poisson's ratio, Young's and bulk moduli, of an aggregate of JST-made or RHO-made spheres arranged in a simple cubic lattice as a function of the volume fraction φ of the nanoporous skeleton.

On the other hand, the normalized first Lamé parameter shows a negative value for small volume fractions $\pi/6 < \varphi < 0.575$. Since $\lambda < 0$ for the constitutive material, λ_p is positive in such a range, while it shares the sign of λ as the volume fraction increases. We note that while a negative first Lamé parameter is not usual, it is thermodynamically possible. Indeed, such a behavior can be explained, from a viewpoint of continuum elasticity, by a smaller material's resistance to volumetric changes (characterized by the bulk modulus) in comparison with resistance to shape changes (determined by the shear moduli). This feature is also connected with the exhibited JST's auxeticity, i.e. a negative Poisson's ratio, which appears to be common in chiral lattices (see e.g.[66,67]) and in over two thirds of the materials with cubic symmetry studied in.[68] In the present case, the Poisson's ratio of the porous solid

is positive for the volume fraction range $\pi/6 < \varphi < 0.575$. This means that the auxetic behavior of the JST substrate is preserved only for larger volume fractions (i.e. for highly consolidated materials instead of arrays of barely overlapping spheres). In addition, the Poisson's ratio for $\pi/6 < \varphi < 0.575$ is close to zero, which indicates that the material does not change in thickness when stretched or compressed. This result highlights the possibility of tuning the mechanical behavior by introducing an extra-scale porosity in the nanoporous solids.

Regarding the behavior of the RHO-based double porosity material, its normalized first Lamé parameter and shear moduli are increasing functions of the volume fraction. The mechanical parameters also show this trend. In particular, it is observed that the normalised bulk modulus takes smaller values than the normalised Poisson's ratio, while the opposite trend is observed for the JST-based material. This is attributed to the auxeticity of the latter. Moreover, the behavior of the mechanical parameters of the RHO-based double porosity material appears similar to that of poroelastic solids with comparable substrate material elastic properties (cf. Figure 9 in this paper and figures 13.4-6 in[50]).

Finally, Figure 10 shows the φ-dependent longitudinal and transversal acoustic velocities in the double porosity material normalized by the respective velocities (i.e. v_{L} and v_{T}) of the nanoporous substrate material calculated using equations 17 and 18, respectively.

$$\frac{v_{\mathrm{L}}^{dp}}{v_{\mathrm{L}}} = \frac{1}{\sqrt{\varphi}}\sqrt{\frac{\lambda_p + 2\mu_{p2}}{\lambda + 2\mu}} \tag{17}$$

$$\frac{v_{\mathrm{T}}^{dp}}{v_{\mathrm{T}}} = \frac{1}{\sqrt{\varphi}}\sqrt{\frac{\mu_{p1}}{\mu}}. \tag{18}$$

The longitudinal and transverse speeds of sound in the porous material increases with an increase in the volume fraction of the nanoporous material. Moreover, it is observed that the normalized longitudinal velocity in the JST-based material is higher than that of the RHO-based material, while the opposite trend is observed for the transversal velocity.

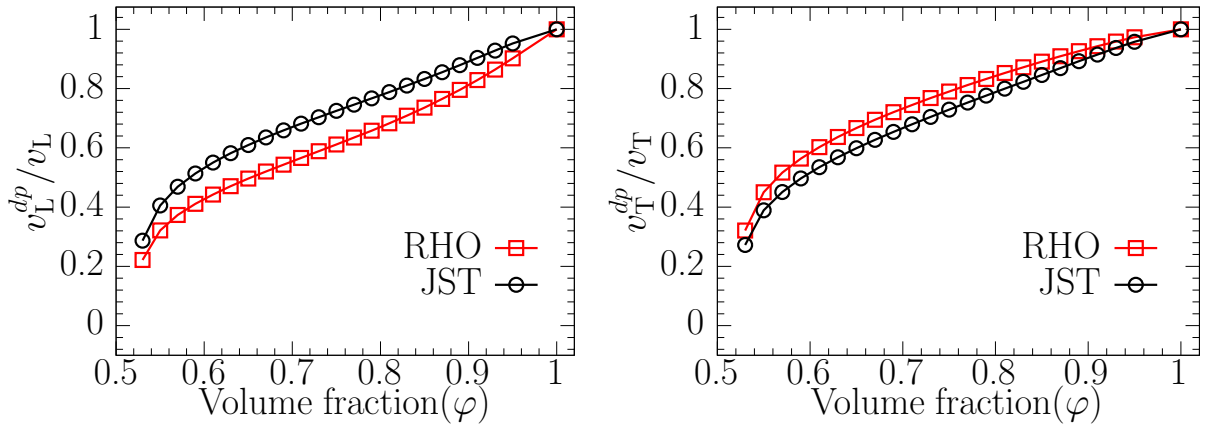

Figure 10: Normalized longitudinal (left) and transverse (right) speeds of sound of an aggregate of JST- or RHO-made spheres arranged in a simple cubic lattice as a function of the volume fraction φ of the nanoporous skeleton.

Taking into account these remarks, it is clear that the possibility of tailoring the acoustic wave propagation in the double porosity medium by adjusting the volume fraction of the nanoporous material is not exclusive to the JST-based double-porosity medium but rather a general possibility enabled by adding an extra scale of porosity to a nanoporous skeleton. The results, thus, demonstrate great flexibility to modulate the acoustic wave propagation in the porous material which provides unprecedented functionality for designing novel acoustic devices with versatile applications.

As a final remark, it is stressed that the upscaling procedure yielded a macroscopic model for anisotropic media but has been exemplified for media with cubic symmetry. The upscaled model and adopted approach can be directly applied to double porosity media whose microstructure exhibits other types of symmetry, including materials such as MOFs.[35,36,69] However, to fully identify the respective effective elasticity tensor $\mathbf{a}$ it is required to both apply successively six macroscopic loadings, i.e. three loadings in pure extensions (i.e. E_{11}, E_{22}, E_{33}) and three loadings in pure shear (i.e. E_{12}, E_{23}, E_{31}), in the boundary-value problem given by Eqs. (42)–(43) and use Eq. (12). Depending on the symmetry of the materials' microstructure fewer loadings may be required, as it is the case for the cubic media studied in this work.

4. Conclusion

We investigated acoustic wave propagation in nanoporous materials using molecular dynamics simulations for prototypical samples of this class of solids. By considering two all-silica zeolites (RHO and JST), we analyze the material acoustics at the nanoscale using a multiscale approach. First, we evaluate the sound velocities from (i) the phonon spectrum of the materials as assessed using the dynamic structure factor and (ii) the macroscopic elastic constants assessed using either a strain-fluctuation approach or simple mechanical tests. The low-frequency peaks obtained in the dynamic structure factor calculations were fitted against a damped harmonic oscillator to predict the sound velocity of the longitudinal and transverse acoustic waves along the (100), (110) and (111) directions. With the strain-fluctuation method, the instantaneous dimensions of the zeolite systems were saved for estimating the mechanical constants by allowing the length and angles of the supercell to change over time. In an alternate approach, the zeolite structures were subjected to different mechanical tests, *i.e.* tensile and shear tests. From the tensile test, the mechanical constants C_{11} and C_{12} were determined by deforming the zeolite along the axial direction. The elastic constant C_{44} was determined by applying a shear deformation to the upper surface of the zeolite while keeping the lower surface fixed to its position. Using the mechanical constants obtained from the mechanical routes, we calculated the direction-dependent longitudinal and transverse speeds of sound by solving Kelvin-Christoffel's equation.

The acoustic velocities predicted by the different approaches showed good agreement in all directions of wave propagation considered in the study. The propagation speed of the acoustic wave in RHO zeolite is found higher due to the higher elastic stiffness when compared to the JST structure. The sound velocities predicted for the RHO zeolite show considerable variation among different wave propagation directions for both the longitudinal and transverse modes. The departure from the isotropic acoustic behavior for RHO zeolite is indicated by a Zener ratio higher than 1. On the other hand, a quasi-isotropic behavior of the JST zeolite revealed by a Zener ratio approximately equal to unity gives rise to almost

similar speeds of sound in different wave propagation directions. The mechanical parameters and the degree of anisotropy of the elastic behavior, therefore, strongly influence the acoustic properties in the nanoporous material. In a second step, using the microscopic data obtained by means of molecular simulation, we proposed a bottom-up modelling strategy to predict the acoustic properties of an empty double-porosity solid. By considering an assembly of slightly overlapping spheres made of a nanoporous skeleton, we propose a simple model to mimic the acoustic properties of materials exhibiting large defects or microfractures. Using this nano-to-macro approach, we illustrate how the acoustic properties of materials can be modulated using hierarchical porous structures and devices. The present work paves the way for future developments with promising perspectives. First, while we chose prototypical materials corresponding to zeolites with cubic structures, the multiscale approach – consisting of molecular simulations and continuum-level calculations – can be extended to other Bravais crystalline lattices. With more complex crystalline structures, the calculation of mechanical parameters is more involved as it involves a much larger number of elastic constants but their estimation does not add complexity. Similarly, considering aluminosilicate zeolites would remain doable despite the need to add a proper description of the interactions with extra-framework cations.

Appendix

A. Dynamic structure factor

In this appendix, we derive the general formula for the dynamic structure factor $S(\mathbf{q}, \omega)$ which can be obtained from the positions or, equivalently, the velocities of the particles in the system.[70] The density distribution $\rho(\mathbf{r}, t)$ at position $\mathbf{r}$ and time t of a system made up of N particles is given by a sum of Dirac delta functions centered on each particle position

$\mathbf{r}_i(t)$:

$$\rho(\mathbf{r},t) = \sum_{i=1}^{N} \delta[\mathbf{r} - \mathbf{r}_i(t)]. \tag{19}$$

We now introduce the generalized Van Hove correlation function $G(\mathbf{r},t)$ which corresponds to the probability distribution that particle i is in the vicinity of $\mathbf{r}$ at time t while particle j is in the vicinity of $\mathbf{r} = 0$ at time t=0.

$$G(\mathbf{r},t) = \left\langle \frac{1}{N} \sum_{i=1}^{N} \sum_{j=1}^{N} \delta(\mathbf{r} - [\mathbf{r}_j(t) - \mathbf{r}_i(0)]) \right\rangle \tag{20}$$

$$= \left\langle \frac{1}{N} \int \mathrm{d}\mathbf{r}' \sum_{i=1}^{N} \sum_{j=1}^{N} \delta[\mathbf{r}' - \mathbf{r} + \mathbf{r}_j(t)] \delta[\mathbf{r}' + \mathbf{r}_i(0)] \right\rangle.$$

As discussed in the main text, the intermediate coherent scattering function $F(\mathbf{q},t)$ is defined as the spatial Fourier transform of the Van Hove correlation function:

$$F(\mathbf{q},t) = \int G(\mathbf{r},t)\ \exp(-i\mathbf{q}\cdot\mathbf{r})\mathrm{d}\mathbf{r} = \frac{1}{N} \left\langle \rho_{\mathbf{q}}(t)\rho_{-\mathbf{q}}(0) \right\rangle, \tag{21}$$

where $\rho_{\mathbf{q}}(t) = \int \rho(\mathbf{r},t) \exp(-i\mathbf{q}\cdot\mathbf{r})\mathrm{d}\mathbf{r} = \sum_{i=1}^{N} \exp[-i\mathbf{q}\cdot\mathbf{r}_i(t)]$. $F(\mathbf{q},t)$ is a very fundamental quantity as it is directly the time Fourier transform of the dynamic structure factor which is probed using neutron scattering for instance:

$$S(\mathbf{q},\omega) = \frac{1}{2\pi} \int_{-\infty}^{+\infty} F(\mathbf{q},t) e^{i\omega t} \mathrm{d}t. \tag{22}$$

In what follows, we show that the dynamic structure factor can be related to the Fourier components of the particle flux $\mathbf{j}_{\mathbf{q}}(t) = \sum_{i=1}^{N} \mathbf{u}_i(t) \exp[-i\mathbf{q}\cdot\mathbf{r}_i(t)]$ (where $\mathbf{u}_i(t)$ is the velocity of molecule i at time t). The condition of particle number conservation in each space direction a can be written in Fourier space: $-i\mathbf{q}\cdot\mathbf{j}_{\mathbf{q}}(t) = \dot{\rho}_{\mathbf{q}}(t)$ where the 'dot' symbol denotes time derivative. By considering the component a (x, y or z) of the dot product in this relation

[i.e. $\dot{\rho}^a_{\mathbf{q}} = -iq^a j^a_{\mathbf{q}}$], we can define the following time correlation function:

$$C_a(\mathbf{q},t) = \frac{1}{N}\left\langle \dot{\rho}^a_{\mathbf{q}}(t)\dot{\rho}^a_{-\mathbf{q}}(0)\right\rangle = \frac{q^2}{N}\left\langle j^a_{\mathbf{q}}(t)j^a_{-\mathbf{q}}(0)\right\rangle . \tag{23}$$

where $q = |\mathbf{q}|$ is the norm of the wave vector $\mathbf{q}$. By noting that $C_a(\mathbf{q},t) = -\mathrm{d}^2F_a(\mathbf{q},t)/\mathrm{d}t^2$ we can write that:

$$C_a(\mathbf{q},\omega) = \omega^2 F_a(\mathbf{q},\omega) = \omega^2 S_a(\mathbf{q},\omega), \tag{24}$$

where the second equality is obtained by considering that $S_a(\mathbf{q},\omega) = F_a(\mathbf{q},\omega)$ by definition. Finally, using the definition of $C_a(\mathbf{q},\omega) = 1/2\pi \int_{-\infty}^{+\infty} C_a(\mathbf{q},t)\exp(i\omega t)\mathrm{d}t$
$= 1/2\pi \int_{-\infty}^{+\infty} q^2/N \left\langle j^a_{\mathbf{q}}(t)j^a_{-\mathbf{q}}(0)\right\rangle \exp(i\omega t)\mathrm{d}t$, Eq. (24) leads to:

$$S_a(\mathbf{q},\omega) = \frac{1}{2\pi N}\left(\frac{q}{\omega}\right)^2 \int_{-\infty}^{+\infty} \left\langle j^a_{\mathbf{q}}(t)j^a_{-\mathbf{q}}(0)\right\rangle e^{i\omega t}\mathrm{d}t, \tag{25}$$

where we recall that $a = x$, y or z.

B. Mechanical fluctuations

For a system in the isobaric-isostress ensemble (constant $N\sigma T$), the free enthalpy is the thermodynamic potential that is minimum at equilibrium: $G = U - \Omega_0 \sum_{\mathrm{ij}} \sigma_{\mathrm{ij}}\epsilon_{\mathrm{ij}} - TS$ where the double sum runs over the three directions of space x, y, and z for both i and j. In this equation, U, S ϵ_{ij}, and Ω_0 are the internal energy, entropy, strain component ij, and volume of the system, respectively. From a statistical mechanics point of view, considering the underlying distribution of microstates in this ensemble, $\rho_{N\sigma T} \sim e^{-\beta G}$ where $\beta = 1/k_{\mathrm{B}}T$, any fluctuation ΔU, ΔS, $\Delta\epsilon_{\mathrm{ij}}$ with respect to the equilibrium solution occurs with a probability $P \sim \exp(-\beta\Delta G)$:

$$P\left(\Delta U, \Delta S, \Delta\epsilon_{\mathrm{ij}}\right) \sim \exp[-\beta(\Delta U - T\Delta S - \Omega_0 \sum_{\mathrm{ij}} \sigma_{\mathrm{ij}}\Delta\epsilon_{\mathrm{ij}})]. \tag{26}$$

From now on, we use Einstein's convention so that summation over repeated indices is implicitly assumed. By writing a second-order Taylor expansion of ΔU, we obtain:

$$\Delta U \sim \frac{\partial U}{\partial S}\Delta S + \frac{\partial U}{\partial \epsilon_{\rm ij}}\Delta\epsilon_{\rm ij} + \frac{1}{2}\frac{\partial^2 U}{\partial S^2}\Delta S^2 + \frac{1}{2}\frac{\partial^2 U}{\partial \epsilon_{\rm ij}^2}\Delta\epsilon_{\rm ij}^2 + \frac{\partial^2 U}{\partial \epsilon_{\rm ij}\partial S}\Delta\epsilon_{\rm ij}\Delta S, \tag{27}$$

where all partial derivatives are taken while keeping constant all other variables. Replacing ΔU from Eq. (27) into Eq. (26) yields:

$$P \sim \exp\left[-\frac{\beta}{2}\left(\frac{\partial^2 U}{\partial S^2}\Delta S^2 + \frac{\partial^2 U}{\partial \epsilon_{\rm ij}^2}\Delta\epsilon_{\rm ij}^2 + 2\frac{\partial^2 U}{\partial \epsilon_{\rm ij}\partial S}\Delta\epsilon_{\rm ij}\Delta S\right)\right], \tag{28}$$

where we used that $\partial U/\partial S = T$ and $\partial U/\partial \epsilon_{ij} = \Omega_0\sigma_{ij}$.

At this stage, we also invoke the following expansion in S and ϵ_{ij} for ΔT and $\Omega\Delta\sigma_{ij}$:

$$\Delta T = \Delta\left(\frac{\partial U}{\partial S}\right) \sim \frac{\partial^2 U}{\partial S^2}\Delta S + \frac{\partial^2 U}{\partial S\partial \epsilon_{\rm ij}}\Delta\epsilon_{\rm ij}, \tag{29}$$

$$\Omega_0\Delta\sigma_{\rm ij} = \Delta\left(\frac{\partial U}{\partial \epsilon_{\rm ij}}\right) \sim \frac{\partial^2 U}{\partial \epsilon_{\rm ij}^2}\Delta\epsilon_{\rm ij} + \frac{\partial^2 U}{\partial S\partial \epsilon_{\rm ij}}\Delta S. \tag{30}$$

The last two expressions allow us to rewrite Eq. (28) as:

$$P \sim \exp\left[-\frac{\beta}{2}\left(\Delta T\Delta S + \Omega_0\Delta\sigma_{\rm ij}\Delta\epsilon_{\rm ij}\right)\right]. \tag{31}$$

In order to express P as a function of simple measurable quantities, we can express the fluctuation in entropy S as:

$$\begin{aligned}\Delta S &= \frac{\partial S}{\partial T}\Delta T + \frac{\partial S}{\partial \epsilon_{\rm ij}}\Delta\epsilon_{\rm ij} \\ &= \frac{C_\epsilon}{T}\Delta T + \frac{\partial S}{\partial \epsilon_{\rm ij}}\Delta\epsilon_{\rm ij} = \frac{C_\epsilon}{T}\Delta T - \Omega_0\frac{\partial \sigma_{\rm ij}}{\partial T}\Delta\epsilon_{\rm ij},\end{aligned} \tag{32}$$

where $C_\epsilon = T\partial S/\partial T|_{\epsilon_{ij}}$ is the heat capacity at constant ϵ_{ij}. In the second equality, we simply use that $\mathrm{d}F = -S\mathrm{d}T + \Omega_0\sigma_{ij}\mathrm{d}\epsilon_{ij}$ and then invokes Maxwell relations $\partial^2 F/\partial T\partial\epsilon_{ij} =$

$\partial^2 F/\partial\epsilon_{ij}\partial T$ to show that $-\partial S/\partial\epsilon_{ij}|_T = \Omega_0\partial\sigma_{ij}/\partial T|_{\epsilon_{ij}}$. Similarly, we can express the change in the stress component σ_{ij} as:

$$\Delta\sigma_{\rm ij} = \frac{\partial\sigma_{\rm ij}}{\partial T}\Delta T + \frac{\partial\sigma_{\rm ij}}{\partial\epsilon_{\rm kl}}\Delta\epsilon_{\rm kl}. \tag{33}$$

Inserting the expressions above for ΔS and $\Delta\sigma_{ij}$ into Eq. 31, we get:

$$P \sim \exp\left[-\frac{\beta}{2}\left(\frac{C_\epsilon}{T}\Delta T^2 + \Omega_0\frac{\partial\sigma_{\rm ij}}{\partial\epsilon_{\rm kl}}\Delta\epsilon_{\rm ij}\Delta\epsilon_{\rm kl}\right)\right]. \tag{34}$$

Using the last expression, we can now derive a simple analytical expression for $\Delta\epsilon_{\rm ij}\Delta\epsilon_{\rm kl}$. For a Gaussian distribution $P(x) = (2\pi x_0^2)^{-1/2}\exp(-x^2/2x_0^2)$, we know that $\langle x^2\rangle = \int_\infty^\infty x^2 P(x){\rm d}x = x_0^2$. By applying this definition to Eq. (34) in which we use $x^2 = \Delta\epsilon_{\rm ij}\Delta\epsilon_{\rm kl}$ and $x_0^2 = k_{\rm B}T/\Omega_0 \times \partial\epsilon_{\rm kl}/\partial\sigma_{\rm ij}$, we get:

$$\Delta\epsilon_{\rm ij}\Delta\epsilon_{\rm kl} = \frac{k_{\rm B}T}{\Omega_0}\frac{\partial\epsilon_{\rm kl}}{\partial\sigma_{\rm ij}} = \frac{k_{\rm B}T}{\Omega_0}S_{\rm ijkl}, \tag{35}$$

where the second equality is obtained by invoking the definition of the compliance tensor $S_{\rm ijkl} = \partial\epsilon_{\rm kl}/\partial\sigma_{\rm ij}$.

C. Homogenization procedure

Classical results (see, *e.g.*[50]) on the upscaling of elastic wave propagation in empty porous solids are recalled in this appendix. We use the two-scale asymptotic method of homogenization for periodic media and closely follow the developments in.[50] The porous solid is periodic, with period ℓ, and has a representative elementary volume Ω (see Figure 8) comprising a nanoporous skeleton Ω_s and empty pores Ω_f, meaning that only acoustic wave propagation through the skeleton is accounted for. The skeleton has a volume fraction $\varphi = \Omega_s/\Omega$ and its common boundary with Ω_f is Γ. The separation of scales is ensured provided that ℓ is much larger than the nanoscopic characteristic size and, at the same time, much smaller than the

macroscopic characteristic size L. The latter allows defining a small parameter $\varepsilon = \ell/L \ll 1$ which will be used in the upscaling procedure.

The equations governing the linear dynamics of the porous solid in harmonic regime are the equation of conservation of momentum (36), elastic constitutive law (37) and boundary condition Eq. (38) stating zero normal stress on Γ, together with periodic boundary conditions on opposite faces of the REV.

$$\mathrm{div}(\boldsymbol{\sigma}) = -\rho\omega^2\mathbf{u} \quad \text{in} \quad \Omega_s, \tag{36}$$

$$\boldsymbol{\sigma} = \mathbf{C} : \boldsymbol{\epsilon}(\mathbf{u}) \quad \text{and} \quad \boldsymbol{\epsilon}(\mathbf{u}) = \frac{1}{2}(\nabla\mathbf{u} + (\nabla\mathbf{u})^T), \tag{37}$$

$$\boldsymbol{\sigma}\cdot\mathbf{n} = \mathbf{0} \quad \text{on} \quad \Gamma, \tag{38}$$

where $\mathbf{u}$ is the skeleton displacement, $\boldsymbol{\sigma}$ is the skeleton's stress tensor, $\mathbf{C}$ is the elasticity tensor, $\boldsymbol{\epsilon}(\mathbf{u})$ is the strain tensor, and $\mathbf{n}$ is the outward-pointing vector normal to Γ.

Considering the macroscopic characteristic length L as a reference length, two spatial variables are introduced, namely $\mathbf{x}_* = \mathbf{X}/L$ and $\mathbf{y}_* = \varepsilon^{-1}\mathbf{x}_*$, where $\mathbf{X}$ is the usual spatial variable. Here $\mathbf{x}_*$ and $\mathbf{y}_*$ are dimensionless spatial variables that account for macroscopic and local fluctuations, respectively. Then, introducing the dimensionless quantities $\mathbf{C}_* = \mathbf{C}/C_c$, $\mathbf{u}_* = \mathbf{u}/u_c$, $\rho_* = \rho/\rho_c$, and $\omega_* = \omega/\omega_c$ (with quantities with subscript $_c$ being respective characteristic values) into Eqs. (36)–(38) lead to the dimensionless local equations (36)–(38) but with the variables indexed by $_*$ and the dimensionless number $\mathcal{P} = |\rho_c\omega_c^2 L^2|/|C_c| = O(1)$ multiplying the inertial term in the equation of conversation of momentum. Further noting that the introduction of the two spatial variables lead to the spatial derivative to take the form $\nabla \to \nabla_x + \varepsilon^{-1}\nabla_y$, where the subscript $_*$ is dropped to simplify the notation from now on, and looking for the unknown variables in the form of asymptotic expansions of powers of ε, *e.g.* $\mathbf{u} = \sum_{i=0}^{\infty}\varepsilon^i\mathbf{u}^{(i)}$, one successively obtains boundary-value problems after inserting the said series into the dimensionless local equations and collecting terms with equal powers of ε.

The lowest order provides a boundary-value problem for $\mathbf{u}^{(0)}$, which reads as

$$\mathrm{div}_y(\mathbf{C} : \boldsymbol{\epsilon}_y(\mathbf{u}^{(0)})) = 0 \quad \text{in} \quad \Omega_s, \tag{39}$$

$$(\mathbf{C} : \boldsymbol{\epsilon}_y(\mathbf{u}^{(0)})) \cdot \mathbf{n} = 0 \quad \text{on} \quad \Gamma. \tag{40}$$

As shown in,[50] the solution of this homogeneous linear problem is

$$\mathbf{u}^{(0)} = \mathbf{u}^{(0)}(x) = \mathbf{U}. \tag{41}$$

Hence the leading-order displacement is a macroscopic variable, i.e. it is constant at the local scale.

Further identification allows obtaining the boundary value problem for $\mathbf{u}^{(1)}$, which is given by (with $\mathbf{E} = \boldsymbol{\epsilon}_x(\mathbf{U})$)

$$\mathrm{div}_y(\mathbf{C} : (\mathbf{E} + \boldsymbol{\epsilon}_y(\mathbf{u}^{(1)}))) = \mathbf{0} \quad \text{in} \quad \Omega_s, \tag{42}$$

$$\mathbf{C} : (\mathbf{E} + \boldsymbol{\epsilon}_y(\mathbf{u}^{(1)})) \cdot \mathbf{n} = \mathbf{0} \quad \text{on} \quad \Gamma. \tag{43}$$

The solution of this linear problem forced by the macroscopic strain $\mathbf{E}$ is given by[50]

$$\mathbf{u}^{(1)} = \boldsymbol{\xi}(y) : \mathbf{E} + \bar{\mathbf{u}}^{(1)}(x) \quad \text{i.e.} \quad u_i^{(1)} = \xi_i^{kh} E_{kh} + \bar{u}_i^{(1)}, \tag{44}$$

where $\boldsymbol{\xi}(y)$ is a zero-spatial-mean third-rank tensor and $\bar{\mathbf{u}}^{(1)}(x)$ is an arbitrary constant. We note that ξ_i^{kh} represents the i-th component of the microscopic displacement in response to a macroscopic strain excitation $\mathbf{E} = \frac{1}{2}(\mathbf{e}_k \otimes \mathbf{e}_h + \mathbf{e}_h \otimes \mathbf{e}_k)$.

The collection of terms at ε leads to the following equations

$$\mathrm{div}_y(\boldsymbol{\sigma}^{(1)}) + \mathrm{div}_x(\boldsymbol{\sigma}^{(0)}) = -\omega^2 \rho \mathbf{U} \quad \text{in} \quad \Omega_s, \tag{45}$$

$$\boldsymbol{\sigma}^{(1)} \cdot \mathbf{n} = 0 \quad \text{on} \quad \Gamma, \tag{46}$$

which after integration, application of the divergence theorem, and use of the periodicity become the following macroscopic equation of conservation of momentum

$$\mathrm{div}_x \boldsymbol{\Sigma} = -\omega^2 \varrho \mathbf{U} \tag{47}$$

where $\varrho = \varphi\rho$ is the effective density, $\boldsymbol{\Sigma} = \langle \boldsymbol{\sigma}^{(0)} \rangle = \mathbf{a} : \mathbf{E}$ (with $\langle \cdot \rangle = \Omega^{-1} \int_{\Omega_s} \cdot d\Omega$) is the effective stress tensor, and the effective elasticity tensor $\mathbf{a}$ is defined in Eq. (12).

In summary, the macroscopic description is given by Eq. (47). The associated effective parameters are ϱ and $\mathbf{a}$ which depends on the elasticity tensor of the skeleton, the volume fraction of the skeleton, and the spatially averaged microscopic strain resulting from a macroscopic strain excitation. To obtain the latter, the solution of the boundary value problem Eq. (42)–(43) for a given $\mathbf{E}$ is required.

Supporting Information Available

Additional data showing the bulk modulus as a function of the framework density for zeolites. This material is available free of charge via the Internet at http://pubs.acs.org.

Conflict of interest

The authors declare that they have no conflict of interest.

Acknowledgement

This work, which was selected as an IRGA project from Univ. Grenoble Alpes and Universidad Austral de Chile, is supported by the French National Research Agency in the framework of the "Investissements d'Avenir" program (ANR-15-IDEX-02) and the Chilean Na-

tional Agency for Research and Development (ANID) through FONDECYT Regular Grant 1211310. Calculations were performed using the Froggy platform of the GRICAD infrastructure (https://gricad.univ-grenoble-alpes.fr), which is supported by the Rhône-Alpes region (GRANT CPER07-13 CIRA) and the Equip@Meso project (reference ANR-10- EQPX-29-01) of the programme Investissements d'Avenir supervised by the French Research Agency. The authors wish to thank Matthieu Vandamme for useful discussions on mechanical calculations.

References

(1) Van Der Voort, P.; Leus, K.; De Canck, E. *Introduction to Porous Materials*; John Wiley & Sons, 2019.

(2) Coasne, B.; Galarneau, A.; Pellenq, R. J.; Di Renzo, F. Adsorption, intrusion and freezing in porous silica: the view from the nanoscale. *Chem. Soc. Rev.* **2013**, *42*, 4141–4171.

(3) Thommes, M.; Kaneko, K.; Neimark, A. V.; Olivier, J. P.; Rodriguez-Reinoso, F.; Rouquerol, J.; Sing, K. S. Physisorption of gases, with special reference to the evaluation of surface area and pore size distribution (IUPAC Technical Report). *Pure Appl. Chem.* **2015**, *87*, 1051–1069.

(4) Bocquet, L.; Charlaix, E. Nanofluidics, from bulk to interfaces. *Chem. Soc. Rev.* **2010**, *39*, 1073–1095.

(5) Huber, P. Soft matter in hard confinement: phase transition thermodynamics, structure, texture, diffusion and flow in nanoporous media. *J. Phys. Condens. Matter* **2015**, *27*, 103102.

(6) Coasne, B.; Gubbins, K. E.; Pellenq, R. J.-M. Temperature effect on adsorp-

tion/desorption isotherms for a simple fluid confined within various nanopores. *Adsorption* **2005**, *11*, 289–294.

(7) Hung, F. R.; Coasne, B.; Santiso, E. E.; Gubbins, K. E.; Siperstein, F. R.; Sliwinska-Bartkowiak, M. Molecular modeling of freezing of simple fluids confined within carbon nanotubes. *J. Chem. Phys* **2005**, *122*, 144706.

(8) Van Speybroeck, V.; Hemelsoet, K.; Joos, L.; Waroquier, M.; Bell, R. G.; Catlow, C. R. A. Advances in theory and their application within the field of zeolite chemistry. *Chem. Soc. Rev.* **2015**, *44*, 7044–7111.

(9) Ackley, M. W.; Rege, S. U.; Saxena, H. Application of natural zeolites in the purificatiand separation of gases. *Microporous Mesoporous Mater.* **2003**, *61*, 25–42.

(10) Misaelides, P. Application of natural zeolites in environmental remediation: A short review. *Microporous Mesoporous Mater.* **2011**, *144*, 15–18.

(11) Mumpton, F. A. La roca mágica: Uses of natural zeolites in agriculture and industry. *Proc. Natl. Acad. Sci. U.S.A.* **1999**, *96*, 3463–3470.

(12) Kosinov, N.; Gascon, J.; Kapteijn, F.; Hensen, E. J. Recent developments in zeolite membranes for gas separation. *J. Membr. Sci.* **2016**, *499*, 65–79.

(13) Tran, Y. T.; Lee, J.; Kumar, P.; Kim, K.-H.; Lee, S. S. Natural zeolite and its application in concrete composite production. *Compos. B. Eng.* **2019**, *165*, 354–364.

(14) Hazen, R. Zeolite molecular sieve 4A: anomalous compressibility and volume discontinuities at high pressure. *Science* **1983**, *219*, 1065–1067.

(15) Colligan, M.; Forster, P. M.; Cheetham, A. K.; Lee, Y.; Vogt, T.; Hriljac, J. A. Synchrotron X-ray powder diffraction and computational investigation of purely siliceous zeolite Y under pressure. *J. Am. Chem. Soc.* **2004**, *126*, 12015–12022.

(16) Chapman, K. W.; Halder, G. J.; Chupas, P. J. Guest-dependent high pressure phenomena in a Nanoporous metal- organic framework material. *J. Am. Chem. Soc.* **2008**, *130*, 10524–10526.

(17) Coasne, B.; Haines, J.; Levelut, C.; Cambon, O.; Santoro, M.; Gorelli, F.; Garbarino, G. Enhanced mechanical strength of zeolites by adsorption of guest molecules. *Phys. Chem. Chem. Phys.* **2011**, *13*, 20096–20099.

(18) Tse, J.; Klug, D.; Ripmeester, J.; Desgreniers, S.; Lagarec, K. The role of non-deformable units in pressure-induced reversible amorphization of clathrasils. *Nature* **1994**, *369*, 724–727.

(19) Huang, Y.; Havenga, E. A. Why do zeolites with LTA structure undergo reversible amorphization under pressure? *Chem. Phys. Lett.* **2001**, *345*, 65–71.

(20) Haines, J.; Levelut, C.; Isambert, A.; Hébert, P.; Kohara, S.; Keen, D. A.; Hammouda, T.; Andrault, D. Topologically ordered amorphous silica obtained from the collapsed siliceous zeolite, silicalite-1-F: a step toward "perfect" glasses. *J. Am. Chem. Soc.* **2009**, *131*, 12333–12338.

(21) Greaves, G.; Meneau, F.; Sapelkin, A.; Colyer, L.; Ap Gwynn, I.; Wade, S.; Sankar, G. The rheology of collapsing zeolites amorphized by temperature and pressure. *Nat. Mater.* **2003**, *2*, 622–629.

(22) Isambert, A.; Angot, E.; Hébert, P.; Haines, J.; Levelut, C.; Le Parc, R.; Ohishi, Y.; Kohara, S.; Keen, D. A. Amorphization of faujasite at high pressure: an X-ray diffraction and Raman spectroscopy study. *J. Mater. Chem.* **2008**, *18*, 5746–5752.

(23) Haiss, W. Surface stress of clean and adsorbate-covered solids. *Rep. Prog. Phys.* **2001**, *64*, 591.

(24) Chen, M.; Coasne, B.; Derome, D.; Carmeliet, J. Coupling of sorption and deformation in soft nanoporous polymers: Molecular simulation and poromechanics. *J. Mech. Phys. Solids* **2020**, *137*, 103830.

(25) Nikoosokhan, S.; Vandamme, M.; Dangla, P. A poromechanical model for coal seams saturated with binary mixtures of CH4 and CO2. *J. Mech. Phys. Solids* **2014**, *71*, 97–111.

(26) Gor, G. Y.; Huber, P.; Bernstein, N. Adsorption-induced deformation of nanoporous materials—a review. *Appl. Phys. Rev.* **2017**, *4*, 011303.

(27) Vermorel, R.; Pijaudier-Cabot, G. Enhanced continuum poromechanics to account for adsorption induced swelling of saturated isotropic microporous materials. *Eur. J. Mech. A/Solids* **2014**, *44*, 148–156.

(28) Brochard, L.; Vandamme, M.; Pellenq, R.-M. Poromechanics of microporous media. *J. Mech. Phys. Solids* **2012**, *60*, 606–622.

(29) Venegas, R.; Umnova, O. Acoustical properties of double porosity granular materials. *J. Acoust. Soc. Am.* **2011**, *130*, 2765–2776.

(30) Venegas, R.; Boutin, C.; Umnova, O. Acoustics of multiscale sorptive porous materials. *Phys. Fluids* **2017**, *29*, 082006.

(31) Miller, Q. R.; Nune, S. K.; Schaef, H. T.; Jung, K. W.; Denslow, K. M.; Prowant, M. S.; Martin, P. F.; McGrail, B. P. Microporous and flexible framework acoustic metamaterials for sound attenuation and contrast agent applications. *ACS Appl. Mater. Interfaces* **2018**, *10*, 44226–44230.

(32) Wright, J. R. The virtual loudspeaker cabinet. *J AUDIO ENG SOC* **2003**, *51*, 244–247.

(33) Bechwati, F.; Avis, M.; Bull, D.; Cox, T.; Hargreaves, J.; Moser, D.; Ross, D.; Umnova, O.; Venegas, R. Low frequency sound propagation in activated carbon. *J. Acoust. Soc. Am.* **2012**, *132*, 239–248.

(34) Jiang, Y.-W.; Xu, D.-P.; Kwon, J.-H.; Jiang, Z.-X.; Kim, J.-H.; Hwang, S.-M. Analysis and application of zeolite in microspeaker box. *J. Mech. Sci. Technol* **2019**, *33*, 3679–3683.

(35) Sun, Y.; Li, Y.; Tan, J.-C. Liquid intrusion into zeolitic imidazolate framework-7 nanocrystals: exposing the roles of phase transition and gate opening to enable energy absorption applications. *ACS Appl. Mater. Interfaces* **2018**, *10*, 41831–41838.

(36) Sun, Y.; Rogge, S. M.; Lamaire, A.; Vandenbrande, S.; Wieme, J.; Siviour, C. R.; Van Speybroeck, V.; Tan, J.-C. High-rate nanofluidic energy absorption in porous zeolitic frameworks. *Nat. Mater.* **2021**, *20*, 1015–1023.

(37) Destgeer, G.; Sung, H. J. Recent advances in microfluidic actuation and micro-object manipulation via surface acoustic waves. *Lab Chip* **2015**, *15*, 2722–2738.

(38) Kelkar, P. U.; Kim, H. S.; Cho, K.-H.; Kwak, J. Y.; Kang, C.-Y.; Song, H.-C. Cellular auxetic structures for mechanical metamaterials: A review. *Sensors* **2020**, *20*, 3132.

(39) Wang, Z.; Hu, H. Auxetic materials and their potential applications in textiles. *Text. Res. J.* **2014**, *84*, 1600–1611.

(40) Scarpa, F. Auxetic materials for bioprostheses [In the Spotlight]. *IEEE Signal Process. Mag.* **2008**, *25*, 128–126.

(41) Boutin, C.; Venegas, R. Assessment of the effective parameters of dual porosity deformable media. *Mech. Mater.* **2016**, *102*, 26–46.

(42) Auriault, J.; Boutin, C. Deformable porous media with double porosity. Quasi-statics. I: Coupling effects. *Transp. Porous Media* **1992**, *7*, 63–82.

(43) Berryman, J. G.; Wang, H. F. The elastic coefficients of double-porosity models for fluid transport in jointed rock. *J. Geophys. Res. Solid Earth* **1995**, *100*, 24611–24627.

(44) Auriault, J.; Boutin, C. Deformable porous media with double porosity III: Acoustics. *Transp. Porous Media* **1994**, *14*, 143–162.

(45) Boutin, C.; Royer, P. On models of double porosity poroelastic media. *Geophys. J. Int.* **2015**, *203*, 1694–1725.

(46) Pride, S. R.; Berryman, J. G. Linear dynamics of double-porosity dual-permeability materials. I. Governing equations and acoustic attenuation. *Phys. Rev. E* **2003**, *68*, 036603.

(47) Rohan, E.; Naili, S.; Cimrman, R.; Lemaire, T. Multiscale modeling of a fluid saturated medium with double porosity: Relevance to the compact bone. *J. Mech. Phys. Solids* **2012**, *60*, 857–881.

(48) Wilson, R.; Aifantis, E. C. On the theory of consolidation with double porosity. *Int. J. Eng. Sci.* **1982**, *20*, 1009–1035.

(49) Parrinello, M.; Rahman, A. Strain fluctuations and elastic constants. *J. Chem. Phys.* **1982**, *76*, 2662–2666.

(50) Auriault, J.; Boutin, C.; Geindreau, C. Homogenization of Coupled Phenomena in Heterogenous Media, ISTE Ltd and John Wiley & Sons. *Inc., London* **2009**,

(51) Baerlocher, C. Database of zeolite structures. *http://www.iza-structure.org/databases/* **2008**, Last accessed on 05/03/2023.

(52) Thompson, A. P.; Aktulga, H. M.; Berger, R.; Bolintineanu, D. S.; Brown, W. M.; Crozier, P. S.; in 't Veld, P. J.; Kohlmeyer, A.; Moore, S. G.; Nguyen, T. D.; *et al.*, LAMMPS - a flexible simulation tool for particle-based materials modeling at the atomic, meso, and continuum scales. *Comput. Phys. Commun.* **2022**, *271*, 108171.

(53) Ghysels, A.; Moors, S. L.; Hemelsoet, K.; De Wispelaere, K.; Waroquier, M.; Sastre, G.; Van Speybroeck, V. Shape-selective diffusion of olefins in 8-ring solid acid microporous zeolites. *J. Phys. Chem. C* **2015**, *119*, 23721–23734.

(54) Hockney, R. W.; Eastwood, J. W. *Computer simulation using particles*; CRC Press, 2021.

(55) Siddorn, M.; Coudert, F.-X.; Evans, K. E.; Marmier, A. A systematic typology for negative Poisson's ratio materials and the prediction of complete auxeticity in pure silica zeolite JST. *Phys. Chem. Chem. Phys.* **2015**, *17*, 17927–17933.

(56) Mizuno, H.; Mossa, S.; Barrat, J.-L. Acoustic excitations and elastic heterogeneities in disordered solids. *Proc. Natl. Acad. Sci. U.S.A.* **2014**, *111*, 11949–11954.

(57) Assuming that the particle density oscillates as a damped harmonic oscillator, the intermediate scattering function is determined, for each $\mathbf{q}$, by a time-dependent function $a(t)$ that is solution of $\ddot{a}+\Gamma_a\dot{a}+\omega_a^2 a=0$, with initial conditions $a(0)=A$ and $\dot{a}(0)=0$. Note that the $\mathbf{q}$-dependence was omitted to ease the notation. Inserting $a=e^{st}$ into the differential equation yields the characteristic polynomial $s^2+\Gamma_a s+\omega_a^2=0$, whose roots are $s=(1/2)(-\Gamma_a\pm\sqrt{\Delta})$. For $\Delta=\Gamma_a^2-4\omega_a^2<0$, the roots are complex conjugated and lead, after applying initial conditions, to $F(\mathbf{q},t)/A=e^{-\frac{\Gamma_a}{2}t}[\cos(\omega_d t)+(\Gamma_a/2\omega_d)\sin(\omega_d t)]$ with $\omega_d=\sqrt{\omega_a^2-\Gamma_a^2/4}$. Applying the Laplace transform to this expression and letting $s=j\omega$ result in $F(\mathbf{q},\omega)/A=(j\omega+\Gamma_a)/(\omega_a^2-\omega^2+j\omega\Gamma_a)$. Recalling that the dynamic structure factor is real and even in time and is given by $S_a(\mathbf{q},\omega)/S_q=\mathrm{Re}(F(\omega)/S_q)$, with the static structure factor being $S_q=A$, one obtains Eq. (4).

(58) Salençon, J. *Mécanique des milieux continus: Concepts généraux*; Editions Ecole Polytechnique, 2005; Vol. 1.

(59) Mouhat, F.; Coudert, F.-X. Necessary and sufficient elastic stability conditions in various crystal systems. *Phys. Rev. B* **2014**, *90*, 224104.

(60) Bower, A. F. *Applied mechanics of solids*; CRC Press, 2009.

(61) Poloni, R.; Kim, J. Predicting low-k zeolite materials. *J. Mater. Chem. C* **2014**, *2*, 2298–2300.

(62) Zener, C. M.; Siegel, S. Elasticity and Anelasticity of Metals. *J. Phys. Chem.* **1949**, *53*, 1468–1468.

(63) Chapman, A.; Higdon, J. Effective elastic properties for a periodic bicontinuous porous medium. *J. Mech. Phys. Solids* **1994**, *42*, 283–305.

(64) Bouhlel, M.; Jamei, M.; Geindreau, C. Microstructural effects on the overall poroelastic properties of saturated porous media. *Model. Simul. Mater. Sci. Eng.* **2010**, *18*, 045009.

(65) Nunan, K. C.; Keller, J. B. Effective elasticity tensor of a periodic composite. *J. Mech. Phys. Solids* **1984**, *32*, 259–280.

(66) Spadoni, A.; Ruzzene, M. Elasto-static micropolar behavior of a chiral auxetic lattice. *J. Mech. Phys. Solids* **2012**, *60*, 156–171.

(67) Ha, C.; Plesha, M. E.; Lakes, R. Chiral three-dimensional lattices with tunable Poisson's ratio. *Smart Mater. Struct.* **2016**, *25*, 054005.

(68) Baughman, R.; Shacklette, J.; Zakhidov, A.; Stafstrom, S. Negative Poisson's ratios as a common feature of cubic metals. *Nature* **1998**, *392*, 362–365.

(69) Redfern, L. R.; Farha, O. K. Mechanical properties of metal-organic framework. *Chem. Sci.* **2019**, *10*, 10666.

(70) Hansen, J.-P.; McDonald, I. R. *Theory of simple liquids: with applications to soft matter*; Academic Press, 2013.

TOC Graphic